Volume II
Appendix D.8
Debris Transport Analysis

This appendix contains the debris transport analysis used to determine information about the dimensions of the External Tank bipod foam ramp and the conditions in which the foam struck the Orbiter, post-mishap. This data provided inputs into the foam testing conducted at Southwest Research Institute for the foam impact testing.

This is a NASA document and is published here as written, without editing by the Columbia Accident Investigation Board. The conclusions drawn in this report do not necessarily reflect the opinion of the Board; when there is a conflict, the statements in Volume I of the Columbia Accident Investigation Board Report take precedence. While the report contains many recommendations to improve the data used in this type of analysis for future missions, the Board did not adopt every recommendation into the Columbia Accident Investigation Board Report.

Figures & Tables

Debris Transport Analysis

Submitted by NASA Accident Investigation Team
Reynaldo J. Gomez III, Michael Aftosmis, Darby Vicker, Dr. Robert L. Meakin, Phillip C. Stuart, Dr. Stuart E. Rogers, James S. Greathouse, Dr. Scott M. Murman, Dr. William M. Chan, David E. Lee, Gerald L. Condon, and Dr. Timothy Crain

1.0 EXECUTIVE SUMMARY

This report documents the results of the STS-107 Investigation team responsible for characterizing the debris impact on the Orbiter wing during the STS-107 launch. These results provided the inputs for the Orbiter Thermal Protection System Impact Test Team as well as information regarding bipod ramp airloads and characterization of the bipod ramp local flow environment.

The goal of this effort was to characterize the External Tank bipod ramp foam trajectory and subsequent impact on the Orbiter lower wing leading edge at a Mission Elapsed Time (MET) = 81.86 seconds. Determining the mass and impact velocity of the debris that struck the Orbiter was a complex effort requiring the integration of inputs from a number of sources. Inputs from the External Tank (ET) Project and the STS-107 Image Analysis Team were combined with CFD and trajectory analysis tools to determine the mass and impact velocity of the debris that struck the lower Reinforced Carbon Carbon (RCC) surface of the Orbiter left wing. In depth evaluations of the Image analysis products along with CFD simulations were the primary efforts that determined the parameters required to characterize the debris in an enough detail to support impact testing required for the STS-107 investigation.

The bipod ramp aerodynamic loads were assessed using CFD solutions at the STS-107 ascent conditions. These results showed that the air loads on the bipod ramps were well within the design certification limits and were a small fraction of the design limits at the debris release conditions. This implies that a foam ramp without flaws should not have failed due to aerodynamic loads.

Assessments of debris impact velocity potential were performed at a range of Mach numbers along the STS-107 ascent profile. These results showed that the debris release conditions on STS-107 were near the worst case combination of freestream velocity (2324 ft/sec) and dynamic pressure (482 psf), from a debris impact velocity perspective.

Three-dimensional trajectories from the launch films and videos were screened using a physics-based trajectory fit based on a steady state flowfield model generated using high fidelity Computational Fluid Dynamics (CFD) tools. These results refined the most likely range of relative velocities at debris impact to between 775 and 820 feet per second. The debris impact velocity is the difference between the vehicle velocity and the debris velocity as shown in the following equation.

$$\text{Impact Velocity} = \text{Shuttle Velocity} - \text{Debris Velocity}$$

$$775\ (^{ft}/_{sec}) = 2324\ (^{ft}/_{sec}) - 1549\ (^{ft}/_{sec})$$

A parallel effort used a more complex CFD model that included the unsteady rotation of the debris and simulated the effect of the debris on the overall flowfield. These results indicated that an 855 in^3 volume of foam from the –Y bipod ramp would impact the Orbiter wing at approximately 950 feet per second. The unsteady moving body simulations provided insight into the most likely initial conditions for the debris release as well estimates of the debris rotation rate and the effect of the debris on the local pressure distribution. These results show that the 855 in^3 foam volume would require an effective density considerably higher than the allowable foam density to impact at a velocity of 820 ft/sec or that the foam volume was significantly larger than 855 in^3.

These analyses along with the inputs from the Image Analysis Team and the ET Project were used to estimate a range of debris dimensions and corresponding weights for the foam debris. These upper and lower velocity and corresponding weight ranges are listed in Table 1-1 along with one of the debris sizes analyzed during the STS-107 and the values used in RCC impact tests. The STS-107 result corresponds to the debris size and impact location closest to the test article used in the RCC impact tests.

	Transport Analysis Lower Bound	Transport Analysis Upper Bound	Estimate made during STS-107 mission[1]	RCC Impact Test Target Values
Velocity (ft/second)	775	820	720	775
Volume (in^3) ρ_{foam} = 2.4 lb/ft^3	1,025	1,240	1,200	1,200
Weight (lb)	1.42	1.72	1.67	1.67
Incidence Angle (degrees)	Dependent on impact location		21°	20.6°

Table 1-1. Comparison of debris impact parameters.

2.0 Background

2.1 Freestream Conditions

During the STS-107 launch a large piece of debris was observed falling from the External Tank at a MET = 81.699 seconds at the following freestream conditions:

MET	81.7 seconds	
Altitude	6,5820 feet	12.47 miles
Mach number	2.46	
Velocity	2,324.1 feet/second	1,584.6 miles/hour
Dynamic pressure	481.72 lb/ft^2	
Density	1.783e-04 $slug/ft^3$	7.1% Seal level density
Temperature	-88.1°F	
Alpha	2.08 degrees	
Beta	-0.09 degrees	
Inboard elevons	0.26 degrees	
Outboard elevons	-4.85 degrees	

Table 2-1. STS-107 freestream conditions at time of debris release.

The freestream conditions and the vehicle geometry determine the flowfield around the Space Shuttle at the time of the debris release. This flowfield, along with the vehicle acceleration, provides the force that causes the debris to accelerate relative to the Space Shuttle Launch Vehicle. The flowfield density and velocity combine to accelerate the debris and the flowfield direction combined with the aerodynamics of the debris determine the trajectory that the debris will follow.

Figure 2-1 shows that the impact location is approximately 58 feet downstream of the debris release point. Although the downstream distance is 58 feet the SSLV travels more than 370 feet during 0.16 second debris trajectory duration.

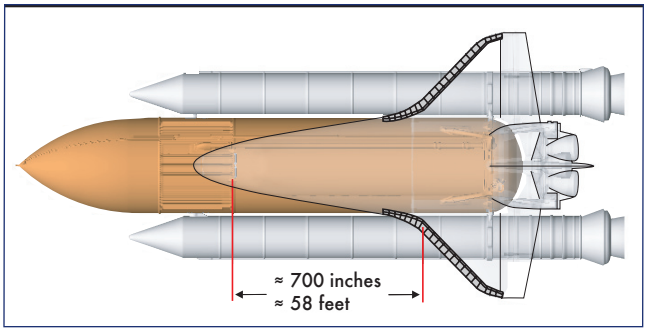

Figure 2-1. Distance from debris source to debris impact location.

At Mach 2.46 the SSLV has transitioned from a negative angle of attack to a positive angle of attack. During the maximum dynamic pressure portion of the ascent profile the SSLV flies at a negative angle of attack to reduce the aerodynamic loads on the Orbiter. Additionally the vehicle has passed the maximum dynamic pressure or max $\bar{q}$, and the region of maximum aerodynamic loading on the vehicle. This data is shown in Figure 2-2.

Figure 2-3 shows that the elevons were moving to their neutral or 0°/0° deflection position during the debris event.

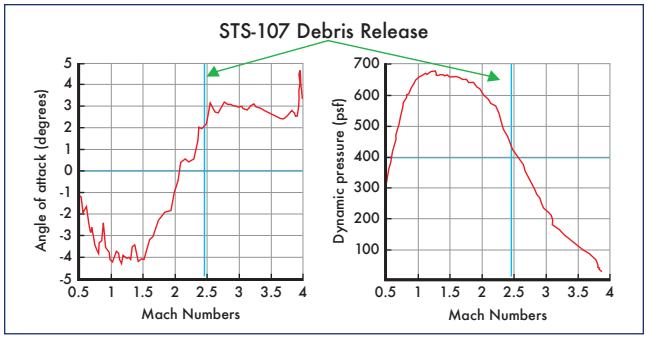

Figure 2-2. STS-107 ascent angle of attack and dynamic pressure history.

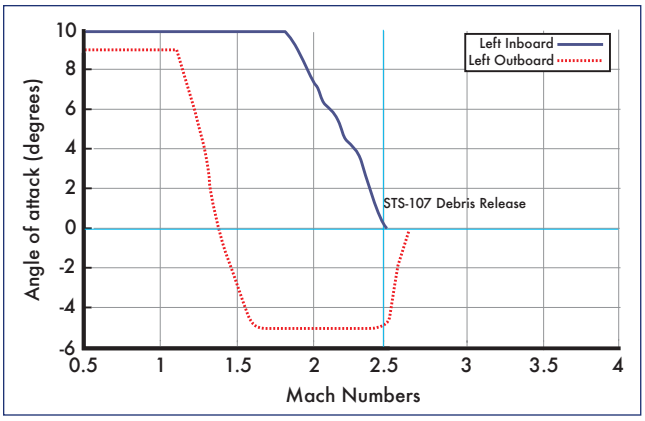

Figure 2-3. STS-107 ascent elevon schedule.

Negative elevon deflections indicate that the elevons are rotated upward, away from the External Tank. The elevon deflection at this point in the ascent trajectory makes debris impacts on the outboard elevon lower surface unlikely.

FIgure 2-4 illustrates the importance of freestream density and velocity on the impact velocity. This figure is based on a constant drag coefficient and does not account for local variations in the flowfield.

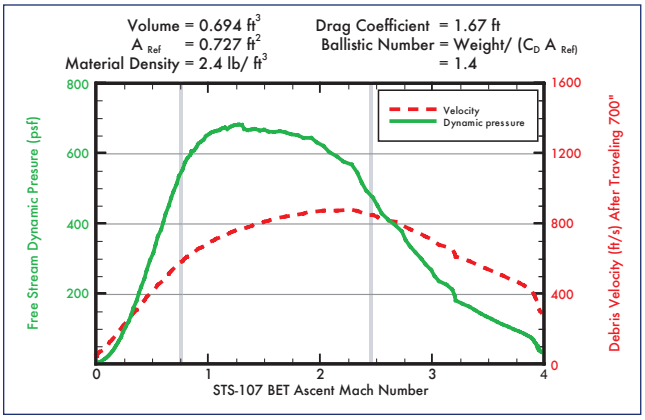

Figure 2-4. Impact velocity vs. Mach number (based on freestream conditions).

Dynamic pressure produces the acceleration force applied to the debris and the freestream velocity determines the maximum relative velocity that the debris can attain. The maximum potential acceleration coincides with the maximum dynamic pressure or max q, which occurred at Mach number = 1.28, however this does not produce the worst case impact velocity. As shown in the previous figure, Mach 2.46 is near the worst case combination of dynamic pressure and freestream velocity in terms of impact velocity potential.

2.2 Debris Transport Background

Typically the size, shape and initial conditions of Space Shuttle ascent debris are unknown. Most debris impacts are assessed after the Shuttle mission ends and the vehicle is inspected on the runway. This is primarily due to the fact that many debris impacts are not visible on ground based launch cameras. Estimating the impact conditions for a specific debris event requires inputs from the Intercenter Photographic Working Group and knowledge of the installed hardware or material at the debris source to refine these assessments. Ideally these inputs would include the following information:

- Debris release time
- Debris source and material properties
- Debris dimensions
- Debris impact location

Currently no single analysis technique can uniquely calculate all of the debris mass and impact conditions. Current Image Analysis tools do not include physical models of the flowfield and debris aerodynamics that would enable them to determine debris mass. The Ascent Debris Transport (ADT) program used to predict debris impact conditions cannot uniquely define debris impact conditions without some knowledge of the debris initial conditions, shape and final velocity. Most debris transport analyses are performed parametrically in an attempt to bound the range of likely debris impact energies for assessment purposes. The ADT program is typically utilized as a statistical tool rather than as an investigative tool. It is useful for looking at ranges of potential debris impacts but it does not have the capability to determine debris volumes and shapes based on an observed trajectory.

Two techniques that have not been employed in previous debris assessments were used to determine the debris mass and drag characteristics. The first technique, discussed in Section 7.0, used physics based trajectory analysis techniques to evaluate three-dimensional trajectories from the Image Analysis Team. The second technique used unsteady moving body CFD codes with the ET Project's maximum estimated foam loss shape to determine the initial conditions required to impact the most likely impact location. It is unlikely that this shape exactly matches the STS-107 debris but it provided a reasonably close shape for evaluation purposes. This is consistent with CFD analysis of various bipod ramp debris shapes that indicated the results are not overly sensitive to the exact debris shape.

2.3 Ballistic Number (BN) Definition

One of the key parameters used to evaluate the mass of the foam debris was the Ballistic Number (BN) sometimes referred to as the ballistic coefficient. This parameter is defined a number of different ways in the literature. In order to avoid confusion the definition used in this document is shown in the following equations.

$$\text{Ballistic Number}\left(\frac{lbs}{ft^2}\right) = \left(\frac{Weight}{C_D A_{ref}}\right) = \left(\frac{Weight}{Drag/Dynamic\ Pressure}\right) \approx \left(\frac{Inertia}{Drag}\right)$$

W = weight (lbs)
C_D = non-dimensional drag coefficient
A_{ref} = reference area (ft2)
$\overline{q}$ = dynamic pressure [???]

Equation 2-1. Ballistic Number (BN) Definition.

Note that the dynamic pressure is shown in terms of local air density (ρ_{local}) and relative velocity ($V^2_{relative}$). The debris and the launch vehicle are in relative motion and consequently the force acting on the debris is proportional to the square of the relative velocity. The local air density is used to account for variation in the flowfield density caused by compressible flow phenomena.

The ballistic number provides an index of the relative sensitivity of an object to aerodynamic forces. The equation shows two different methods for computing the BN: one requires a drag coefficient and a reference area; the other requires measured drag and dynamic pressure. The reference area is typically chosen to correspond to the frontal area of an object or the projected planform area of a wing. The drag coefficient is then calculated based on a measured force where the aerodynamic drag is given by the following equation:

$$\text{Drag force (lb)} = \bar{q}\, C_D A_{ref}$$

Equation 2-2. Drag force equation.

For a tumbling object or an unknown shape the reference area is arbitrary and a C_D value cannot be specified without a definition of the reference area. Fortunately the BN can be calculated without specified values for these variables since the drag force can also be written in the following way:

$$\text{Aerodynamic acceleration} \left(\frac{ft}{sec^2}\right) = \bar{q}\,\frac{g}{BN}$$

$$g = \text{gravitational acceleration} = 32.174 \left(\frac{ft}{sec^2}\right)$$

Equation 2-3. Aerodynamic acceleration due to drag.

The trajectory analysis documented in Section 7 is based on this definition and does not require a specific reference area or drag coefficient. This equation also shows that aerodynamic acceleration is a function of BN. As the ballistic number decreases the drag force and resultant impact velocity increases and as the ballistic number increases the drag decreases and the resultant impact velocity decreases. The Figure 2-5 shows estimated impact velocity vs. ballistic number for a Mach 2.46 flowfield for debris from the bipod region impacting the wing leading edge on RCC panel 8.

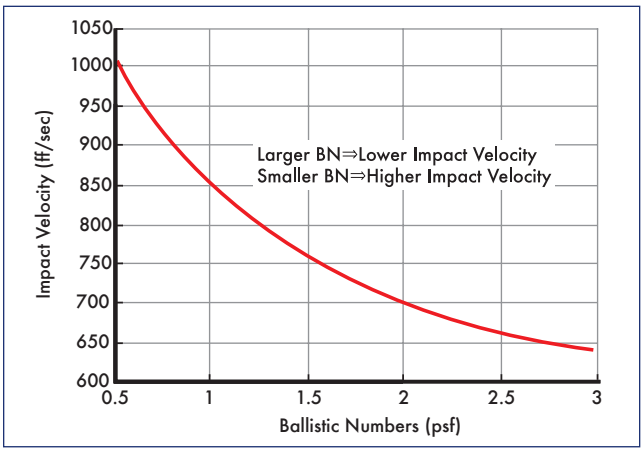

Figure 2-5. Impact velocity vs. ballistic number at STS-107 conditions.

Since the debris is tumbling it has a time varying drag force. This implies that the BN is not a constant but is a function of time. This variation is accounted for in the unsteady CFD analysis in Section 8 and was as documented in Section 7.

2.4 STS-107 Debris Transport Assessment Approach

The overall process consisted of three types of analysis followed by an integration of the results. These steps are listed below:

- Review of relevant inputs from other groups
  - Image Analysis Team
  - ET Project
  - Boeing Debris Transport Program
- Assessment of the STS-107 Image Analysis Team 3-dimensional trajectories using physics based trajectory codes and CFD flowfields
- Simulation of debris trajectories using unsteady 6-DOF CFD codes.
- Integration of results to produce inputs for Southwest Research Institute Impact tests

Results of this analysis included:

- Detailed assessments of the flowfield in the vicinity of the –Y bipod ramp
- Comparisons of these flowfields to wind tunnel and flight data
- Assessment of the Image Analysis impact velocities
- Ranges of most likely impact velocity and incidence angle
- Ranges of most likely debris weights
- Assessment of debris rotational motion

3.0 STS-107 Image Analysis Team Inputs

The STS-107 Image Analysis Team provided inputs that were instrumental in refining the estimated debris size. These results came from a number of different organizations and the ranges shown in the table bracket the results from the various groups that made up the Image Analysis Team. The significant inputs are summarized in Table 3-1 and the following text.

The Image Analysis Team also reported a third debris dimension based on a simplified debris transport analysis by Dwight Divine III of Lockheed-Martin Gaithersburg. The results of this analysis were not used due to the simplified nature of the analysis but the concepts from this analysis were used in the detailed analyses documented in Section 7. These detailed analyses played a key role in evaluating the

Debris release time	MET = 81.699 seconds
Debris source	-Y bipod ramp
Number of impacts	One large debris impact
Impact location	Left wing RCC Panel 5-9 Most likely range 6-8
Impact velocity range	625-840 ft/sec Most likely velocity = 700 ft/sec
Debris dimensions	24″ ± 3″× 15″± 3″
Tumble rate	At least 18 revolutions/second

Table 3-1 Image analysis inputs.

3-dimensional trajectories from the various members of the Image Analysis Team.

One the most important inputs from this group were 3-dimensional trajectories and view vectors extracted from the launch camera film and videos. Four of the trajectories are shown in Figure 3-1. These trajectories provided the reference information needed to narrow the estimated range of the weights and velocities for the debris released from the External Tank. This refinement was required due to the limited number of test articles available for impact testing and the critical nature of these impact tests to determine the foam damage potential.

3.1 Assessment of Impact Analysis Inputs

Based on the initial positions of each of these trajectories and the camera frame rates an initial average velocity can be calculated for each of these trajectories. Figure 3-2 shows the initial positions of four of the 3-dimensional trajectories relative to the bipod ramp. These points are assumed to represent the debris locations 1/2 of a frame (12.25 milliseconds) after release.

The velocities shown are average velocities required to move from the installed location to the first observed debris point. This simple analysis assumes that the debris broke away halfway in time between the last frame before the debris is

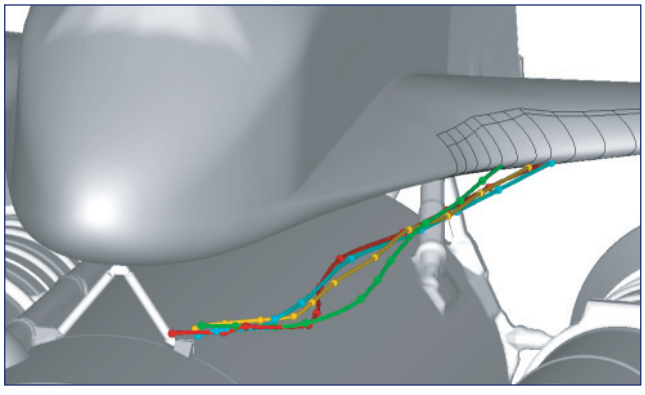

Figure 3-1. Sample set of 3-dimensional trajectories from various members of the Image Analysis Team.

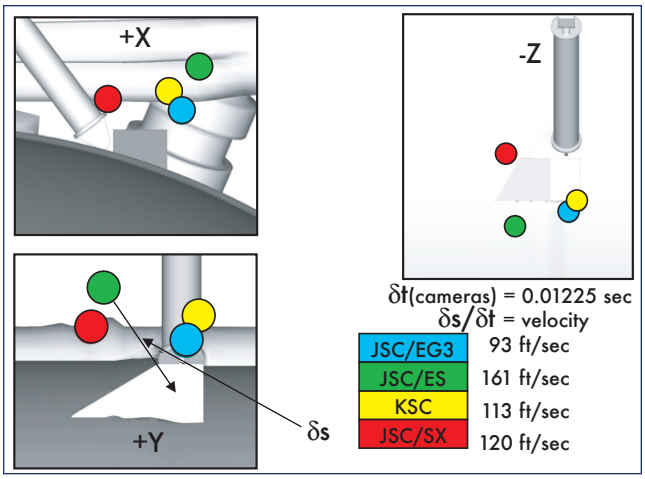

Figure 3-2. Initial trajectory points from Image Analysis Team.

observed to move. It is possible that the debris was released at a slightly different time. A later release time would decrease the δ*t* term and increase the initial velocity estimate. An earlier release time would have the opposite effect.

Note that two of the initial trajectory points shown in the +Y view of Figure 3-2 are actually ahead of the ramp. This implies that the debris somehow moved forward, against the oncoming flow, initially and then traveled aft towards the Orbiter wing. This would require some force acting on the aft edge of the foam ramp that could overcome the aerodynamic forces acting on the ramp at the time of the debris release. Flaws in the bipod ramp shown in Reference 3-2 are in an area where this force could have been applied. However, there is no data on the STS-107 ramp to confirm the existence of similar defects in the STS-107 foam ramps.

The wide range of initial locations and fairly large differences in the observed trajectories could have been caused by optical distortions due to flow gradients caused by shock waves. Shock waves in the bipod vicinity come from the Orbiter and Solid Rocket Boosters. Shock waves ahead of the wing leading edge could have distorted observations of the final portion of the trajectory prior to the debris impact. Images showing the shock waves affecting the bipod region are discussed in Section 5.

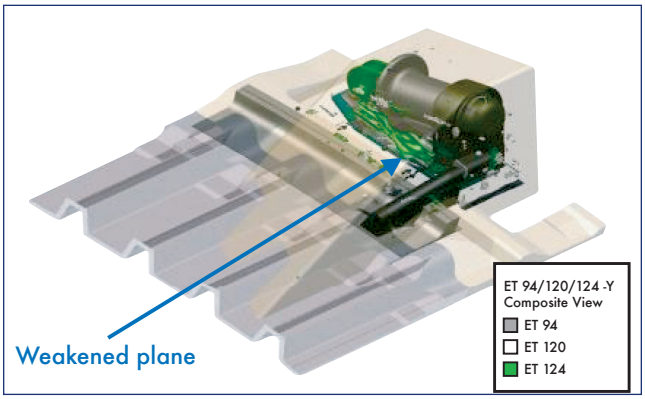

Figure 3-3. Weakened plane in bipod ramp foam.

4.0 External Tank Project Inputs

The External Tank Project provided detailed drawings and material properties for the bipod ramp configuration flown on STS-107. Additionally a Computer Aided Drawing (CAD) model was developed of the outer mold line of the ET that has been incorporated into the latest CFD solutions of the SSLV.

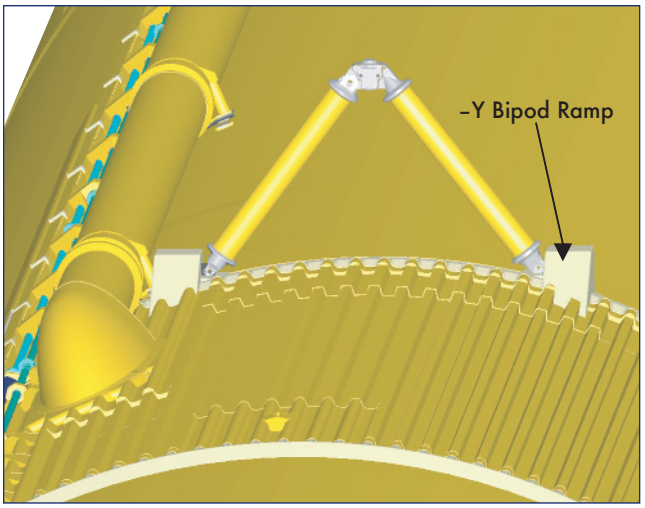

Figure 4-1. ET-93 CAD model detail.

Figure 4-1 includes the bipod struts, LO2 Feedline, cable trays and the stringer geometry ahead of the bipod ramp. These details were not available during the early part of the investigation and most analyses were carried out with simplified geometries that did not include the stringers on the ET Intertank and included simplified representations of the feedline geometry.

4.1 Assessment of External Tank Inputs

The External Tank Project did not have exact measurements for the bipod foam ramp flown on the STS-107 External Tank (ET). The ramp angle on ET93, the tank used on STS-107, was estimated by reviewing closeout photographs to be approximately 25°.

The two primary variables affecting the volume and weight of foam in the bipod ramp are the ramp angle and the BX-250 foam density. The allowable ranges are listed in Table 4-1 below:

	Minimum Allowable	Maximum Allowable
Ramp angle (degrees)	22	30
BX-250 foam density (lb/ft^3)	1.8	2.6

Table 4-1. Allowable range of ramp dimensions and foam densities.

Lower ramp angles increase the volume of foam in the installed ramp. The height remains the same but the length ahead of the bipod strut increases. Measurements from ET94 and ET120, two ETs manufactured at approximately the same time as ET93 had measured ramp angles from 21°-24°. Using similar logic to that used to determine the 855 and 867 in^3 volumes, volume estimates were made for 22 and 30 degree ramp angles, these values are shown in Table 4-2.

Ramp Angle	Max. Volume Loss
22°	1042 in^3
26°	855 in^3
30°	722 in^3

Table 4-2. Estimated maximum foam volume loss vs. bipod ramp angle.

During the STS-107 investigation the ET Project was unable to find any credible scenario that would support the loss of any other hardware or large piece of insulation that would significantly increase the mass of the foam debris.

An estimate was made of the maximum potential foam loss based on this ramp angle. The original estimated maximum foam loss was 855 in^3. Later in the investigation this estimate was increased to 867 in^3. The initial estimate assumed that the thin region aft of the ramp would break off during the debris separation. At a foam density of 2.4 lb/ft^3 these volumes of foam would weigh approximately 1.2 pounds. These estimated volumes are shown in Figures 4-2 and 4-3.

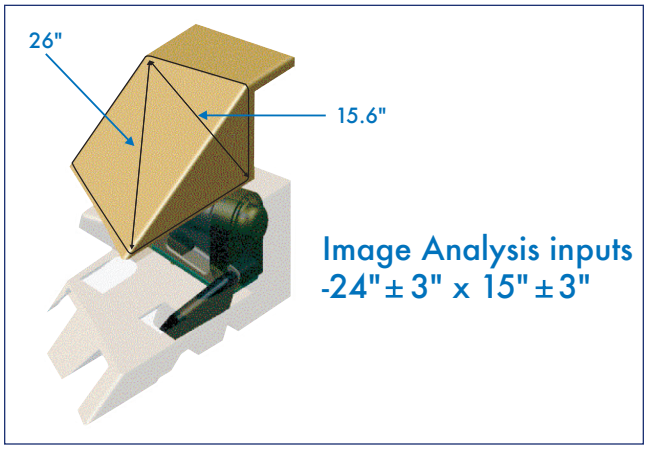

Figure 4-2. Initial maximum estimated foam loss.

The dark outline in Figure 4-2 represents the initial 855 in^3 estimated worst case foam loss. Note that the diagonal dimensions are similar to those reported by the Image Analysis Team. The final estimate included a small amount of Super-Lightweight Ablator SLA.

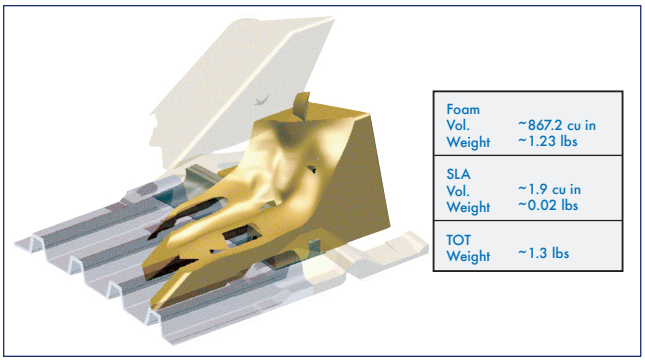

Figure 4-3. Final maximum estimated foam loss.

5.0 Static Geometry CFD Solutions

5.1 Background

Computational Fluid Dynamic (CFD) solutions were used to characterize the flowfield surrounding the Space Shuttle Launch Vehicle (SSLV) at the debris release time. These solutions provided the local aerodynamic acceleration used in the Ascent Debris Transport program and the trajectory analysis used to estimate the debris ballistic number described in Section 7. Additionally these solutions were used compute air loads on the bipod ramp as well as to visualize the flowfield in the bipod vicinity.

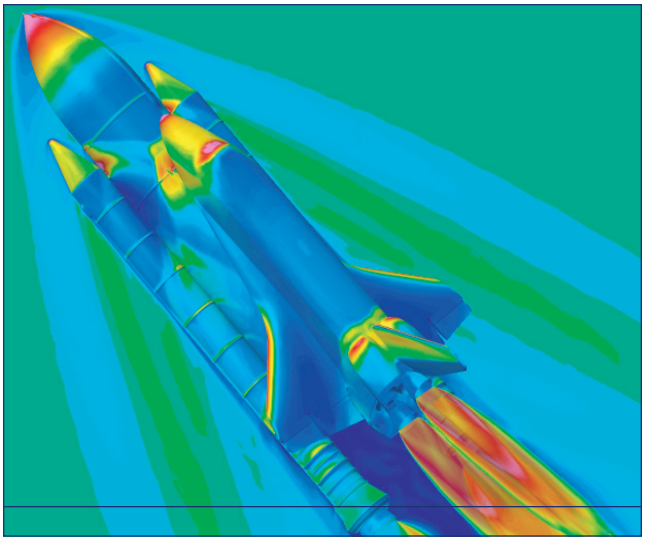

Figure 5-1. Pressure coefficient on the Space Shuttle surface and Mach number in the surrounding flowfield at the STS-107 debris release conditions.

The flowfield in the bipod ramp region, at the STS-107 debris release conditions, has a number of interesting features. Each of the SSLV elements generates a bow shock and the Orbiter and SRB shocks intersect just ahead of the bipod ramp. The left hand SRB shock effect on the local surface pressures is visible as a light blue area in Figure 5-1 on the ET between the SRB nose and the Orbiter nose. These shock-shock interactions with the boundary layer cause the boundary layer ahead of the bipod ramp to separate. Figure 5-2 shows Mach number isosurfaces, colored yellow, at the debris release conditions. These images show the bow shock ahead of the ET as well as the SRB shocks intersecting with the shock off of the Orbiter nose just ahead of the bipod ramps.

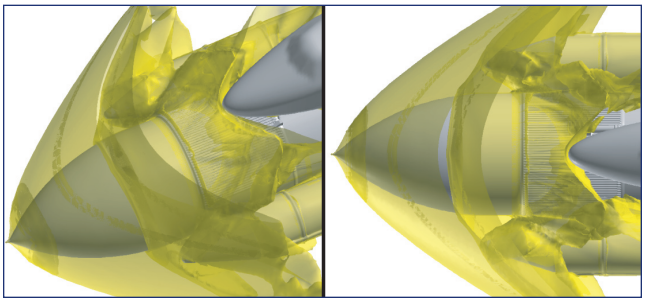

Figure 5-2. Mach number isosurfaces at Mach number = 2.46.

5.2 Solver Background/Verification

The OVERFLOW CFD solver developed by Pieter Buning/NASA Langley Research Center was used to produce these CFD simulations. OVERFLOW is a structured (overset) grid, Navier-Stokes flow solver. It uses a finite-difference formulation, with flow quantities stored at the grid nodes. OVERFLOW has central- and Roe upwind-difference options, and uses a diagonalized, implicit approximate factorization scheme for the time advance. Local time stepping, multigrid and grid sequencing are used to accelerate convergence to a steady state. In this study, 2nd-order central differencing with Jameson-type 2nd/4th-order scalar dissipation is used. Thin-layer viscous terms are computed in wall-normal directions by default and the Spalart-Allmaras 1-equation turbulence model is used to simulate turbulent phenomena.

OVERFLOW has been extensively validated with flight and wind tunnel data. This is documented in references 5-3 through 5-5. The original development of OVERFLOW was funded by the Space Shuttle Systems Integration Office and focused on the development of a capability to accurately simulate transonic aerodynamic loads on the SSLV. During the investigation these results were compared to wind tunnel, previous Operational Flight Test data and STS-107 ascent pressures with good agreement for all of these comparisons. Typical run times for each of these solutions were on the order 10 hours using 128 processors on an SGI Origin 3900 located at NASA Ames Research Center operated by the NASA Advanced Supercomputing Division.

5.3 Other Applications

Bipod ramp air loads were evaluated using these CFD solutions and compared to the aerodynamic loads certification limits used to design the ramp. These results are shown in Appendix B.

A series of numerical experiments were performed to determine if there was any significant unsteadiness in the bipod ramp region. No measurable unsteadiness was found using

the current grid system but there could be subscale unsteadiness that was not resolved due to the local grid spacing in the bipod region.

Surface constrained flow lines, extracted from the static CFD solution, were used to estimate areas where secondary debris strikes may have been detected by the vehicle pressure sensors. Figure 5-3 shows flow lines on the Orbiter lower surface at the debris release freestream conditions the red regions indicate possible secondary impact locations that might have resulted in anomalous pressure measurements during the vehicle ascent. These locations were determined based on their positions relative to the anomalous pressure tap measurements, the local flow direction and further any damage should not affect any other down stream or adjacent pressure instruments which behaved nominally.

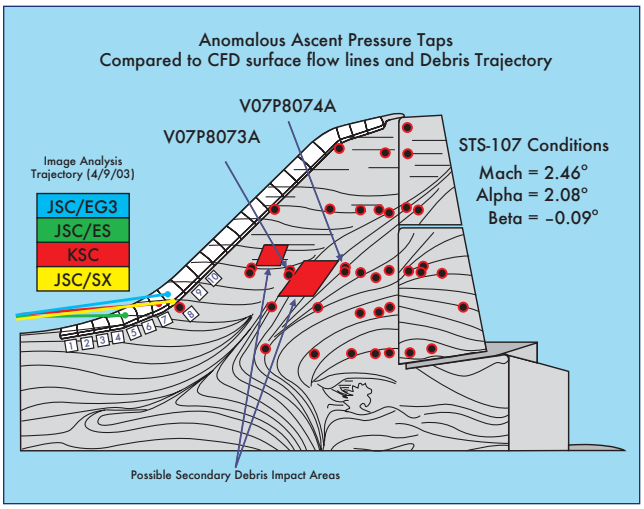

Figure 5-3. Surface flow lines and possible secondary impact locations.

6.0 Ascent Debris Transport Program (ADTP)

The Ascent Debris Trajectory Program is documented in Reference 5-1 and is a Shuttle Systems Design Criteria Critical Math Model (CMM). The following description from CMM 00209 describes the code, its use and required inputs:

> The Debris Trajectory Program is used to calculate the trajectories and resulting impact conditions of ice and other debris particles released from the Space Shuttle during ascent flight, for the purpose of predicting Orbiter tile damage characteristics. The resulting debris impact location and velocity data are used by the Orbiter Project to predict tile impact damage dimensions to determine the acceptability of the debris source for ascent flight and to resolve post-flight debris issues. CFD solutions of the Space Shuttle aerodynamic flowfield are used to calculate the aerodynamic acceleration of the debris as it passes through the flowfield. Required inputs include both debris properties and flight conditions at the time of release.

6.1 Assumptions/Limitations

The ADT program is based on the following assumptions:

1. Debris is tumbling uniformly.
2. Aerodynamic forces act on an area equal to the average area of all exposed surfaces.
3. Aerodynamic drag, gravity and vehicle thrust are the only significant forces acting on the tumbling debris, lift force is not modeled.
4. Debris does not affect the local flowfield.
5. Static flowfields are used; flowfield changes due to vehicle acceleration are not modeled.

Realistically lift forces are relatively large during the initial portion of the trajectory. Initial rotation, during the early portion of the trajectory, has a strong effect on the debris trajectory. Section 7 contains an illustration of the effect of the debris on the local surface pressures as the debris travels down the body.

The program is limited to rectangular solid, circular cylinder and spherical shapes. Approximate solutions can be obtained by selecting the shape most similar to the particle being analyzed. Particle drag coefficient data, as a function of Mach number, is defined for the expected range of Shuttle ascent flight conditions and debris particle sizes corresponding to Reynolds numbers of one or greater. CFD solutions at various conditions are used for parametric debris studies to predict debris impact conditions from subsonic conditions up to Solid Rocket Booster (SRB) separation. When the actual flight conditions at the time of debris release are known CFD flowfield solutions are selected from the available Mach number/angle of attack combinations to bound the time of particle release.

6.2 Code Review Results

During the STS-107 investigation a thorough review of the ADTP was performed. A number of bugs and errors were discovered in the program. The errors included problems in the code's time integration scheme and some incorrect assumptions regarding the input gravity and vehicle acceleration vectors. Additionally several very inefficient routines were identified during this review. Replacement of the inefficient routines resulted in more than 3 orders of magnitude speed improvement in the code along with improved accuracy due to the use of an improved solution interpolation method.

Review of the drag coefficient tables in the ADTP resulted in several findings.

1. Tumbling rectangular solid drag coefficient look up table was actually for a rotating solid disk.
2. Most of the tumbling drag coefficient data dates back to the 1950s and are based on small metal cubes or other simple shapes.
3. The assumption that the reference area is equal to the average exposed surface area not consistent with all of the available drag coefficient data.
4. Update used Hoerner's tumbling cube data for all rectangular solids.

Conventionally the reference area is based on frontal or planform area and the some of the drag tables used in the ADT used planform area rather than average area. This assumption is particularly problematic for thin flat plates, disks or high aspect ratio objects. Using an average area where the drag coefficient is based on a planform area will result in an under prediction of the drag force and result in a lower impact velocity.

Review of this material showed that the there are relatively few sources of information for tumbling debris drag coefficients and that most of the sources are quite old and for very small objects. This is an area that could benefit from additional wind tunnel and CFD analysis.

The static CFD solution described in section 5 was used with the corrected code to obtain a more accurate prediction of the foam debris impact conditions on STS-107. These results are compared to the predictions made during the STS-107 mission in the next sub section.

6.3 Results compared to STS-107 Mission Predictions

During the STS-107 three different foam debris sizes were analyzed. One of the debris sizes, a 20″× 10″× x 6″ volume, is within the final estimated range of foam volumes predicted by detailed ballistic number estimates in Section 7. The original predicted impact velocity on RCC Panel 8 was 710 ft/sec with an impact angle of up to 21° as shown in Figure 6-1. These analyses were performed using relatively coarse grid CFD solutions at a Mach number of 2.5 and at angles of attack of 1.5° and 3.0°. These values compare well with the Mach 2.46 and angle of attack of 2.08° values determined by the post STS-107 ascent reconstruction.

Using a high fidelity flowfield at the STS-107 debris release conditions and a 1200 in^3 debris volume, along with the updated/corrected ADT, resulted in an impact velocity of 830 ft/sec. This result is within 55 ft/sec of the final estimated velocity used in the impact testing performed at the Southwest Research Institute. The final impact test used an angle of incidence equal to 20.6° that was quite close to the 21° value shown in the previous figure.

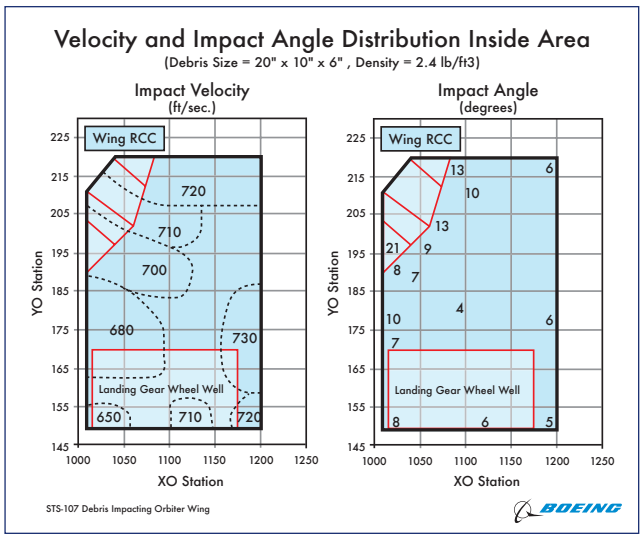

Figure 6-1. STS-107 debris impact results.

7.0 Trajectory Analysis/Ballistic Number Determination

This section details attempts to model the motion of the large debris object that apparently separated from the STS-107 external tank at approximately 81.7 seconds MET and subsequently impacted the left wing of the Orbiter. These analyses used observational data together with dynamical models to determine likely trajectories and properties of the debris object. Three separate coordinated analyses were performed by Condon, Crain, and Lee.

Condon and Lee both took the approach of using optimizer routines to fit trajectories to observational data based on a least-squares fit. They each performed analyses using two forms of observational data: first three-dimensional points estimated by image analysis groups, and later the "view vector" or "view line" form of data from the image analysis groups. Condon focused on a parametric approach to scan the pre-processed three-dimensional point data sets, using these results and other observation data-quality information to provide a better focus for the follow-on "view vector" analysis. Lee attempted to assess input data and specific case results to identify a "most reliable case" estimate.

Crain approached the problem using the more rigorous methods of statistical epoch state estimation. He applied the batch-least-squares method to estimate trajectory initial conditions and average ballistic number. This approach provided a measure of the uncertainties in the solution parameters that is a function of the uncertainty in the observations and the debris path. The Crain analysis was based on the three-dimensional point sets from image analysis.

7.1 Condon Analysis: Least Squares Optimized with Pre-processed and View Vector Data

This analysis was used to predict the impact velocity of foam debris with the Shuttle wing along with an estimate of the average ballistic number of this debris. The first part of the analysis compared integrated trajectory data to pre-processed imagery data sets acquired from four NASA organizations (JSC/ES, JSC/SX, KSC, and JSC/EG).

7.1.1 Approach Trajectory vs. Pre-processed Imagery Data Sets

This analysis attempts to minimize the sum square distance between time-dependent positions along the propagated foam debris trajectory and time-equivalent corresponding positions estimated from ground imagery data. Both parts of the deterministic trajectory analysis required development of the equations of motion for the foam debris relative to the Shuttle External Tank (ET) coordinate frame (Figure 7-1). The sum of the forces on the Shuttle (m_1) include accelerations due to engine thrust, drag, and gravity. The sum of forces on the debris (m_2) include acceleration from drag

and gravity only. The difference in the acceleration between the Shuttle and the debris, in the Shuttle ET coordinate frame, can be expressed as the difference between the drag acceleration of the debris and the Shuttle Orbiter sensed acceleration (due to thrust and drag). Note that the gravitational acceleration term drops out, as the gravity acting on the Shuttle and the debris are essentially the same. The drag force on the debris is a function of the density (ρ), relative velocity (V_{rel}), the drag coefficient (C_D), and the area (A). If we define the ballistic number (BN) as $m_2 g_0/(C_D A)$, then we can express the acceleration of the debris relative to the Shuttle as a function of the dynamic pressure (q), BN, and the Shuttle sensed acceleration.

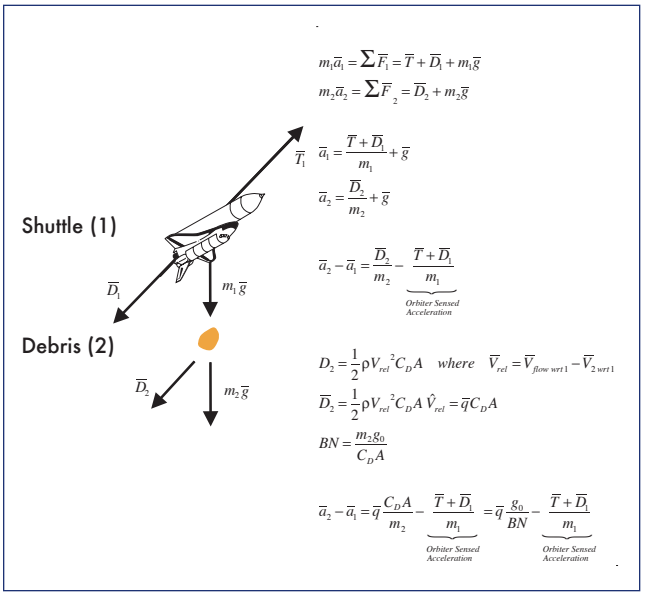

Figure 7-1. Force diagram of Shuttle and foam debris accompanied by associated equations of motion.

The Orbiter sensed acceleration, based on flight data and provided by the JSC/EG3 organization, is assumed to be constant over the approximately 170 milliseconds duration of the foam debris trajectory from the Shuttle bipod to impact on the wing. The sensed acceleration value (at Mach number 2.48) used in the trajectory simulation is:

$$a\_sensed = [-75.163\ -0.058\ -2.472]\ ft/s^2.$$

The foam debris trajectory was propagated using a specially developed MATLAB simulation employing a Runge-Kutta fourth order integrator. The trajectory was integrated through a local velocity flow grid, obtained from JSC/EG3, that provided local velocity vectors, density, and speed of sound as a function of position vector components in the Shuttle ET coordinate frame. The 73x36x21 local velocity flow grid matrix covered the following range of position components (in units of inches):

1100 < x < 1820,	-350 < y < 0,	550 < z < 750
positive nose to tail	positive out right wing	positive through tail

The simulation performs an optimization using MATLAB's FMINCON routine to minimize the sum of the square of the time dependent distances (ΣD_n^2) between the integrated trajectory (Figure 7-2, dashed curve with circular icons) and the predetermined position data sets generated by JSC/ES, JSC/SX, KSC, and JSC/EG (Figure 7-2, solid curve with square icons). These four reference data sets are found in Appendix E.1. The MATLAB FMINCON optimization function employs ΣD_n^2 as the objective function to be minimized using 7 controls: the initial state vector (3 initial position controls and 3 initial velocity controls) and a constant BN over the entire debris trajectory. The initial state and BN are numerically perturbed to minimize the sum of the square of the distances at some or all of 11 data index points.

Imagery data suggested that the debris did not enter full ballistic trajectory behavior until around index point 4 or 5. Prior to that (index points 1-4 or 5), the debris appears to be heavily affected by multi-directional lift and drag accelerations. The equations of motion

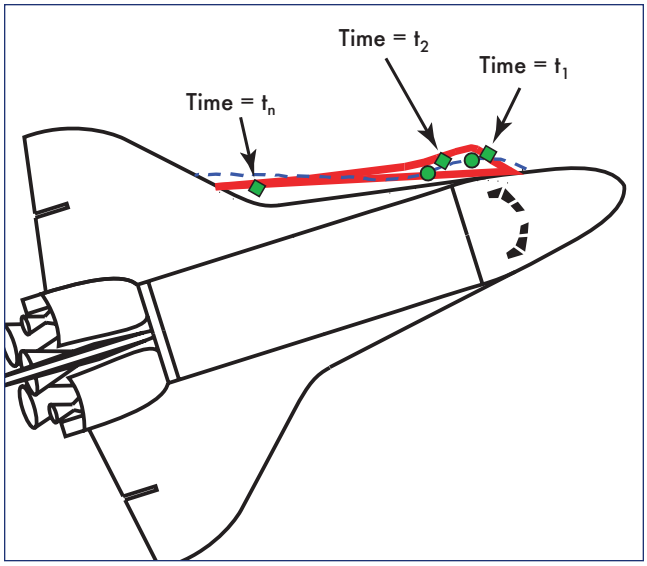

Figure 7-2. Illustration of time-dependent position differences between one of four reference data sets (JSC/ES, JSC/SX, KSC, or JSC/EG) and an integrated trajectory employing a flight-based local velocity flow field. The objective (minimized) function is the sum of the squares of the distances between some or all eleven of these time-dependent position points (ΣD_n^2).

for this part of the analysis employed only drag acceleration and not lift acceleration. For this reason, BN and estimated impact velocity data were generated for trajectories with initial conditions specified in this ballistic debris flow region. Index points 10 and 11 lacked consistent views from one or more (two) camera views, bringing into question the accuracy of the imaging data for these points. Further, preliminary data using the JSC/SX reference database showed relatively consistent BN results in this ballistic flow region away from the lift-affected initial part of the trajectory (index points 1 – 4 or 5) and the questionable end points 10 and 11.
A trajectory comparison analysis was then performed for the region including index points 4 and 5 through 8 and 9 (i.e.,

				Controls							Objective Function (Min)		
				Initial State						Initial Bn			
Data Set	Intervals	Initial Interval Time (sec)	Final Interval Time (sec)	X (in)	Y (in)	Z (in)	Vx (fps)	Vy (fps)	Vz (fps)	Ballistic Number (lb/ft^2)	Sum Square Position Error (in^2)	Average Error per Interval (in^2)	Projected Velocity @ X = 1800 in. (fps)
JSC/ES	4-8	0.050	0.117	1146.73	-151.56	585.43	191.11	-26.58	49.82	2.5134	1207.84	301.96	647
JSC/ES	4-9	0.050	0.133	1149.34	-154.17	585.43	138.61	-10.29	49.85	1.8064	1524.75	304.95	719
JSC/ES	5-8	0.067	0.117	1206.86	-171.86	595.39	96.34	20.44	52.01	1.0854	341.89	113.96	826
JSC/ES	5-9	0.067	0.133	1206.86	-172.32	595.48	94.98	23.35	51.46	1.0782	344.53	86.13	827
JSC/SX	4-8	0.050	0.117	1164.53	-136.26	578.60	-8.72	9.84	59.78	1.2217	623.65	155.91	803
JSC/SX	4-9	0.050	0.133	1164.86	-133.81	579.06	-10.85	-2.14	57.68	1.2168	725.85	145.17	808
JSC/SX	5-8	0.067	0.117	1191.17	-134.75	586.47	83.00	-6.31	66.14	0.8960	451.67	150.56	883
JSC/SX	5-9	0.067	0.133	1190.30	-132.30	587.37	119.10	-23.38	59.52	1.0300	559.47	139.87	847
JSC/EG	4-8	0.050	0.117	1139.89	-116.00	586.27	125.29	-48.72	42.45	1.4103	1215.65	303.91	788
JSC/EG	4-9	0.050	0.133	1134.11	-115.16	586.97	226.07	-56.15	37.72	2.1322	1860.28	372.06	695
JSC/EG	5-8	0.067	0.117	1184.27	-125.81	593.66	224.31	-51.42	42.42	1.1887	1158.66	386.22	823
JSC/EG	5-9	0.067	0.133	1180.98	-124.93	594.49	350.27	-64.02	33.43	2.5056	1804.99	451.25	674
KSC	4-8	0.047	0.109	1168.93	-125.93	583.59	66.63	-45.48	59.27	1.4059	67.62	16.90	772
KSC	4-9	0.047	0.125	1168.57	-126.67	585.00	73.99	-42.20	52.42	1.4516	109.30	21.86	763
KSC	5-8	0.063	0.109	1196.96	-134.85	591.66	183.20	-50.95	61.79	1.2317	46.66	15.55	803
KSC	5-9	0.063	0.125	1196.29	-135.63	593.57	204.68	-47.78	49.41	1.3939	104.83	26.21	771

Table 7-1. BN and projected velocity results for reference data sets (JSC/ES, JSC/SX, JSC/EG3, KSC).

indices 4 – 8, 4 – 9, 5 – 8, and 5 – 9) for each of the reference data sets (JSC/ES, JSC/SX, KSC, and JSC/EG). This analysis produced constant BN values and associated projected impact velocities as shown in Table 7-1. A key comment would be to consider the sparse imagery-based trajectory analysis results in the context of the data available. There were only 11 data points presented of which only about 5 or so are useful (without additional lift modeling in the analysis*).

At this point a caveat about this methodology should be mentioned. One must keep in mind that closely matching a trajectory to the reference data with the minimum sum square position error doesn't necessarily mean that the BN and projected impact velocity is the most accurate. The sparse data coupled with the fact that these data sets represent already pre-processed data suggest that the best trajectory match will only be as good as the original data set. With this in mind, the author attempts to temper results by considering overall consistency of the results and the best possible matching of the data to the methodology using as much appropriate data as possible. For example, this methodology employs only a drag model and will show the best results in region of the trajectory where the debris experiences ballistic motion. Early in the trajectory, imaging suggests the existence of lifting on the debris. The maximum number of useful data points should be employed to provide the best possible representation of the actual debris flight. For example, if only two data points are used, the trajectory simulation could produce a nearly zero sum square error. However, with such few data points, the confidence in the resulting BN and projected velocity would be low.

7.1.2 Observations

The limited data resulted many times in large variations in BN. The 11 data points available for analysis were further limited by unusable data points at the beginning of the trajectory due to unmodeled lift and a couple of questionable or unusable data points at the end of the trajectory due to camera viewing limitations or image analysis limitations.

The KSC data set (see Table 7-1) for ranges (4-8, 4-9, 5-8, and 5-9) produced the most consistent BN values. Trajectory optimization using the KSC reference data set resulted in a BN ranging from 1.2317 – 1.4516 lb/ft^2 and an associated projected velocity range (at X=1800 inches) of 763 – 803 ft/s. These ranges represent approximately an 18% variation in BN and a 5% variation in predicted velocity at X = 1800 in. (near impact location). The minimum sum square error of all assessed data sets is 15.55 in^2 per interval in the index interval range 5-8. A 3-dimensional plot of the trajectory positions and the reference data set positions for this portion of the debris trajectory (Figure 7-3) reflects the low sum square

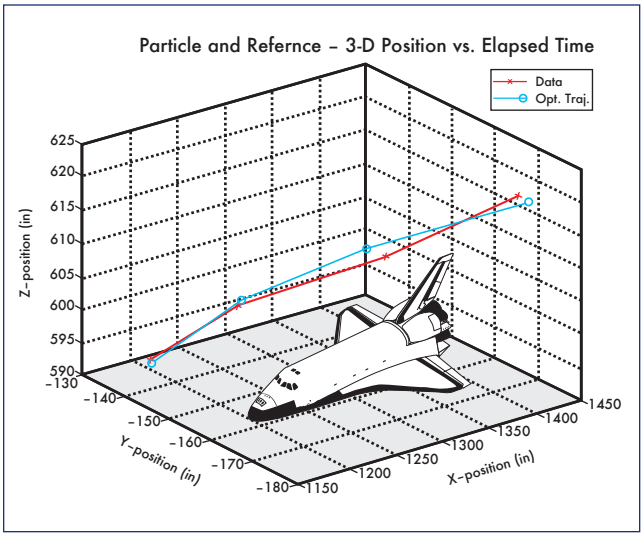

Figure 7-3. Three-dimensional view of foam debris trajectory as compared to KSC reference data for index range (5-8). Note: Shuttle diagram is for attitude reference only and is not to scale.

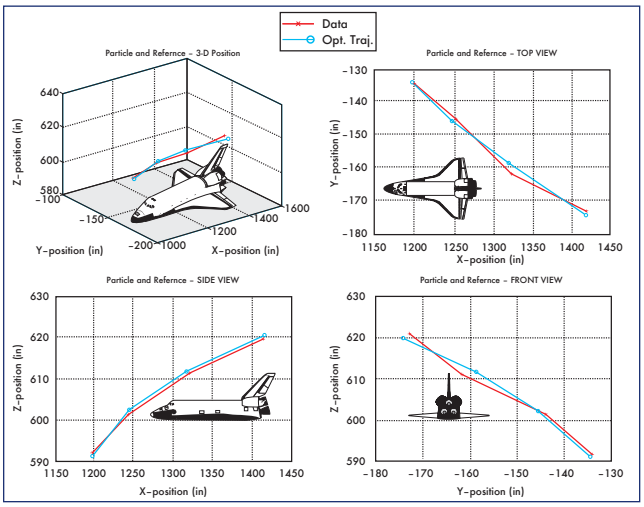

Figure 7-4. Composite view of foam debris trajectory as compared to KSC reference data for index range (5-8) including top, side and "front" views. Note: Shuttle diagram is for attitude reference only and is not to scale.

error. A composite view of the 3-D plus front, side, and top views of the trajectory comparison are shown in Figure 7-4.

The time tags for the JSC/ES, JSC/SX, and JSC/EG data are consistent with each other and with that of a 60 frame/second camera. The first 10 points of the KSC data appear to be taken from a 64 frame/second camera. The interval between the last two KSC data points (10 and 11) is approximately 140% that of a normal 64 frame/second rate and may be spurious. Convergence of trajectories including the 11th reference data point results in high BN values. Other, more consistent data (previously described) suggest these high BN values to be erroneous. They were not considered in the results of this analysis. The JSC/SX data carries a higher sum square error over the selected ranges of integration, however these data also appear to be relatively consistent. The BN values range from 1.0300 – 1.2217 lb/ft^2 over the same index interval ranges as that of the KSC data. This BN range is a bit lower than that of the KSC with a slightly wider variation (approximately 19%), while the projected speed at X = 1800 inches ranges from 803 – 883 ft/s representing a 10% variation between the maximum and minimum values. The BN ranges for the JSC/ES and JSC/EG reference data sets were much more varied (133% and 132%, respectively) and the projected velocity values (at X = 1800 inches) carried a variation of 28% and 22%, respectively. The more consistent BN and projected velocity results fostered better confidence in the KSC and JSC/SX reference data sets.

A plot of the projected velocities at X = 1800 inches (Figure 7-5) shows the consistent velocity results for the KSC based data. The JSC/SX velocities appear to be almost as consistent as the KSC data and are uniformly higher than the KSC data. The results for the JSC/ES and JSC/EG are a bit more "choppy". In contrast to the lower sum square error of the KSC data for index interval range 5-8, the JSC/EG carries a higher sum square position error and associated larger differences between the trajectory and the reference data set (see Figures 7-6 and 7-7).

While the previous analysis sought only constant BN values across the trajectory, a preliminary look was given to minimizing the sum square error between the integrated trajectory and the reference data sets using multiple BNs (and the initial state) as controls. This initial look was done with the JSC/ES reference data set, which as more reference data sets became available, appeared to possess less consistent data than other data sets (i.e., KSC and JSC/SX). The data in Table 7-2 shows BN values, sum square error, and the initial state for trajectory optimizations employing both single and

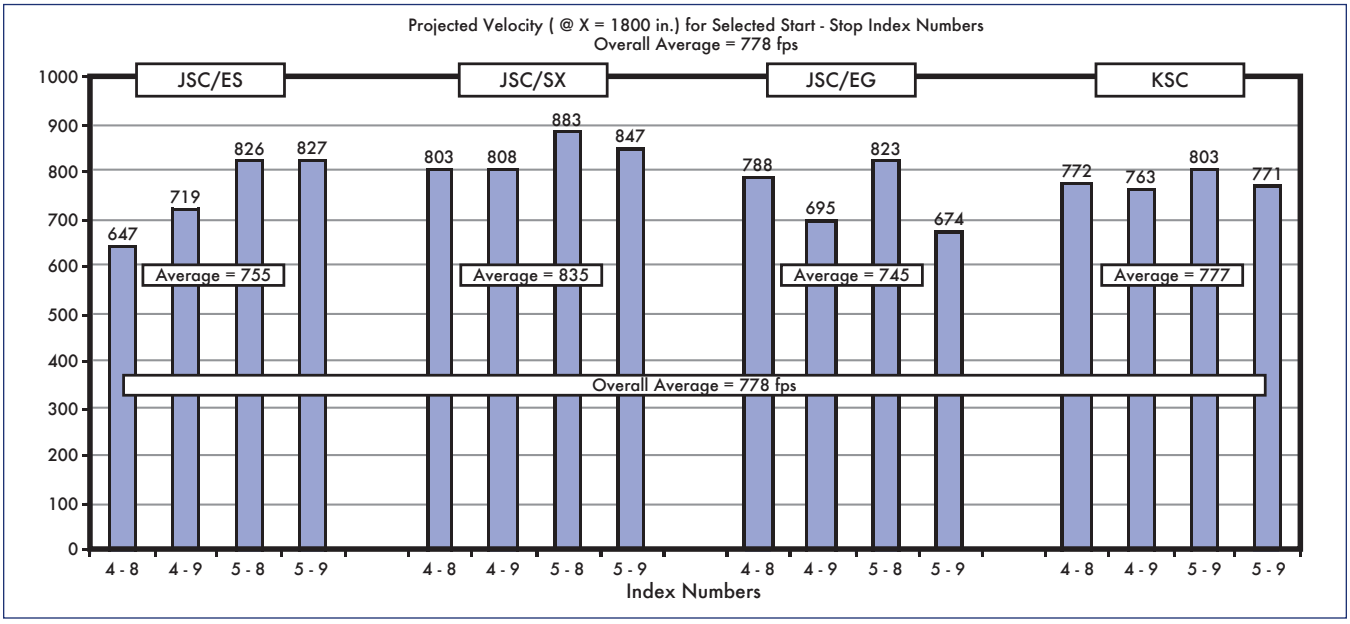

Figure 7-5. Projected velocity of foam debris to position X = 1800 inches, for reference data sets JSC/ES, JSC/SX, JSC/EG, and KSC. The KSC data provides the most consistent projected velocity results.

multiple BN controls. Assumptions used in generation of this particular data include constant local velocity between index intervals and10 internal integration steps between index intervals. While the magnitude of the BNs for the multiple BN trajectories can become exceedingly large, a point of interest to note is that the BNs have a cyclic nature (large to small to large). One could infer from this that the changing BN was a result of a rotating piece of debris. Imagery data confirms this. Further, the multiple BN case using the most data points (i.e., 2-10) indicates a rotation rate of about 20 revolutions/second. This is in relatively good agreement with rotation rates extracted from imagery data.

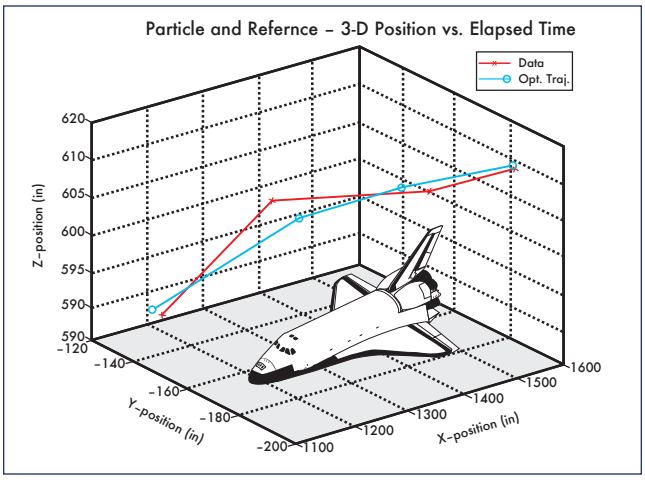

Figure 7-6. Three-dimensional view of foam debris trajectory as compared to JSC/EG reference data for index range (5-8). The sum square position error for this case is larger than that based on the KSC reference data set, as shown in Figure 7-3. Note: Shuttle diagram is for attitude reference only and is not to scale.

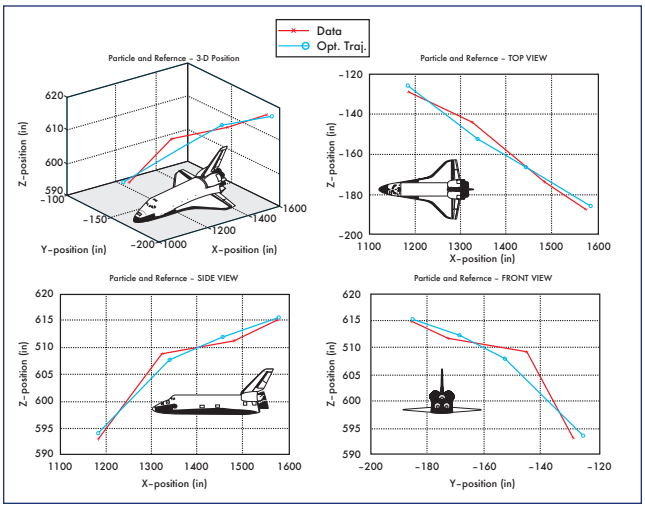

Figure 7-7. Composite view of foam debris trajectory as compared to JSC/EG reference data for index range (5-8) including top, side and "front" views. Note: Shuttle diagram is for attitude reference only and is not to scale.

Index	Elapsed Time (sec)	Single Ballistic Number Optimization Control							Multiple Ballistic Number Optimization Control						
1	0.000	BN1	BN1	BN1	BN1	BN1	BN1	BN1	BN1	BN1	BN1	BN1	BN1	BN1	BN1
2	0.017	BN2	BN2	BN2	BN2	BN2	BN2	BN2	**BN2**	BN2	BN2	BN2	BN2	BN2	BN2
3	0.033	BN3	**BN3**	BN3	BN3	BN3	BN3	BN3	**BN3**	**BN3**	BN3	BN3	BN3	BN3	BN3
4	0.050	BN4	BN4	**BN4**	BN4	BN4	BN4	BN4	**BN4**	**BN4**	**BN4**	BN4	BN4	BN4	BN4
5	0.066	BN5	BN5	BN5	**BN5**	BN5	BN5	BN5	**BN5**	**BN5**	**BN5**	**BN5**	BN5	BN5	BN5
6	0.083	BN6	BN6	BN6	BN6	**BN6**	BN6	BN6	**BN6**	**BN6**	**BN6**	**BN6**	**BN6**	BN6	BN6
7	0.100	BN7	BN7	BN7	BN7	BN7	**BN7**	BN7	**BN7**	**BN7**	**BN7**	**BN7**	**BN7**	**BN7**	BN7
8	0.117	BN8	BN8	BN8	BN8	BN8	BN8	**BN8**	**BN8**	**BN8**	**BN8**	**BN8**	**BN8**	**BN8**	**BN8**
9	0.133	BN9	BN9	BN9	BN9	BN9	BN9	BN9	**BN9**	**BN9**	**BN9**	**BN9**	**BN9**	**BN9**	**BN9**
10	0.150	BN10	BN10	BN10	BN10	BN10	BN10	BN10	**BN10**	**BN10**	**BN10**	**BN10**	**BN10**	**BN10**	**BN10**
11	0.167	BN11	BN11	BN11	BN11	BN11	BN11	BN11	BN11	BN11	BN11	BN11	BN11	BN11	BN11
1	0.000	BN1							1.000	1.000	1.000	1.000	1.000	1.000	1.00
2	0.017	BN2							50.537	1.000	1.000	1.000	1.000	1.000	1.00
3	0.033	BN3	2.15208						1.106	3.474	1.000	1.000	1.000	1.000	1.00
4	0.050	BN4	2.15208	2.28391					5.773	2.251	8.208	1.000	1.000	1.000	1.00
5	0.066	BN5	2.15208	2.28391	1.95284				17.247	42.263	13.833	13.224	1.000	1.000	1.00
6	0.083	BN6	2.15208	2.28391	1.95284	2.58165			1.058	0.671	1.302	0.706	0.298	1.000	1.00
7	0.100	BN7	2.15208	2.28391	1.95284	2.58165	*1000*		1.186	102.181	0.999	1.470	84.813	348.948	1.00
8	0.117	BN8	2.15208	2.28391	1.95284	2.58165	*1000*	*1000*	10.734	1.849	36.370	206.760	302.151	1000.000	729.10
9	0.133	BN9	2.15208	2.28391	1.95284	2.58165	*1000*	*1000*	93.614	17.662	31.179	408.217	263.402	102.980	1000.00
10	0.150	BN10	2.15208	2.28391	1.95284	2.58165	*1000*	*1000*	224.947	55.640	58.044	1000.000	492.291	147.066	889.64
11	0.167	BN11	2.15208	2.28391	1.95284	2.58165	*1000*	*1000*	224.947	55.6405	58.0444	1000	492.291	147.0662	889.637
	$R1_{init}$	in.	1129.08	1144.39	1197.90	1248.13	1318.36	1441.46	1125.14	1128.08	1144.05	1205.13	1258.77	1318.44	1441.47
	$R2_{init}$	in.	-144.64	-160.53	-174.63	-175.62	-177.00	-183.49	-123.65	-144.36	-160.83	-176.29	-177.82	-177.01	-183.49
	$R3_{init}$	in.	581.26	589.52	598.97	607.32	615.84	623.45	575.99	581.66	589.20	598.87	607.49	615.83	623.45
	$V1_{init}$	ft/sec	47.39	190.94	238.56	401.49	582.84	574.02	1.91	94.56	258.35	218.58	-70.03	582.20	573.99
	$V2_{init}$	ft/sec	-0.52	5.79	17.09	-2.30	-22.32	-17.48	-19.60	-6.03	-3.51	20.60	71.50	-22.25	-17.47
	$V3_{init}$	ft/sec	39.07	36.81	35.10	27.41	14.83	3.31	38.40	37.47	37.62	35.32	38.60	14.86	3.31
Least Square Position Error (in.^{2})			3556.74	2149.39	1165.66	960.02	138.85	33.73	4834.65	3142.53	1493.01	464.88	185.90	141.20	33.75

Table 7-2. Single and multiple BN values and initial states for the JSC/ES reference data set. Note that a maximum allowable BN of 1000 was used for the multiple BN cases. On possible explanation for the arbitrarily high BN is the sparseness and uncertainty in the imagery-based data set.

7.1.3 Conclusions

The KSC data set for index ranges (4-8, 4-9, 5-8, 5-9) produced the most consistent results, including the lowest sum square position error as compared to the other data sets (JSC/ES, JSC/SX, and JSC/EG). This data set resulted in the smallest overall sum square error (46.66 in^2) and the smallest sum square error per index interval (15.55 in^2). The average projected velocity of 777 fps was, coincidentally, very close to the overall average of 778 fps for velocity results from all data sets. Based on this KSC data, the ballistic number ranges from 1.23 to 1.45 lb/ft^2 and produce a range of velocities of 763 to 803 fps (at an X-position of 1800 in.).

Note that results for the sampling of multiple BN cases appear to support imaging analysis data indicating foam debris rotation. More abundant and accurate trajectory data may have allowed the trajectory analysis to produce a trust-worthy time history of the actual BN, aiding analysts in better confirming the orientation of the foam debris as well as its trajectory.

7.1.4 Approach –Trajectory vs. View Vector Data

As mentioned in the previous section, comparisons between an integrated trajectory and pre-processed reference data sets may possess inherent errors due to the nature of these data sets (e.g., curve fitting of imagery data, unknown assumptions made by analysts, etc.). A second approach option employing trajectory comparison directly to camera view vector data attempts to generate the most realistic values for BN and projected velocity. This approach minimized the sum square error (in the ET coordinate frame) between an integrated trajectory and view vector data for cameras 208 and 212, obtained from Marshall Space Flight Center. The diagram and equations of motion in Figure 7-1 also apply to this approach. In fact the overall approach for this trajectory vs. view vector data comparison (part 2) is the essentially the same as that of the trajectory vs. reference data sets (part1). The approaches differ in that the sum square error objective (optimization) function in this approach (part 2) is obtained by comparing the integrated trajectory to the perpendicular distance from the camera view vectors for two ground cameras 208 and 212 (see Figure 7-8).

The time stamps for the cameras were not synchronized, so the view vector data had to be interleaved. After performing some analysis using the interleaved data, MSFC noted that the image analysis team achieved much better "triangulation" of the imaging data when the time stamp for camera 208 was shifted earlier by 6.75 milliseconds (milliseconds). Subsequent analysis was performed using the time shifted time stamp for camera 208. The interleaved data for the original and time shifted camera view vector data are shown in Appendix E-2 along with anchor positions and estimated error associated with the view vectors at each index interval point.

The interleaved camera data result in 19 index intervals covering the imaged flight of the foam debris from just after break-away to impact with the Shuttle's port (left) wing. As in part 1, the drag-based modeling in the equations of motion focused the analysis to consideration of the index points beyond the initial points, which appeared to include uncertain flow interactions including lifting. Further, as in part 1, the latter index points were not considered in the analysis due to poor imagery confidence resulting from blocked debris view from one or both cameras. In order to maintain correlation with the start and stop intervals from the part 1 reference data set comparison, a range of candidate trajectory optimizations was selected on the basis of previous results from pre-processed data sets provided by JSC/ES, JSC/SX, JSC/EG, and KSC. Figure 7-9 shows the index interval selection of the view vector data set of part 2 as compared to that of the reference data sets in part 1. For the view vector based analysis the index interval ranges used were 7-13, 7-14, 7-15, 7-16, 8-13, 8-14, 8-15, and 8-16. This ballistic flow region was considered to be the best range for obtaining the best average BN and impact velocity estimates.

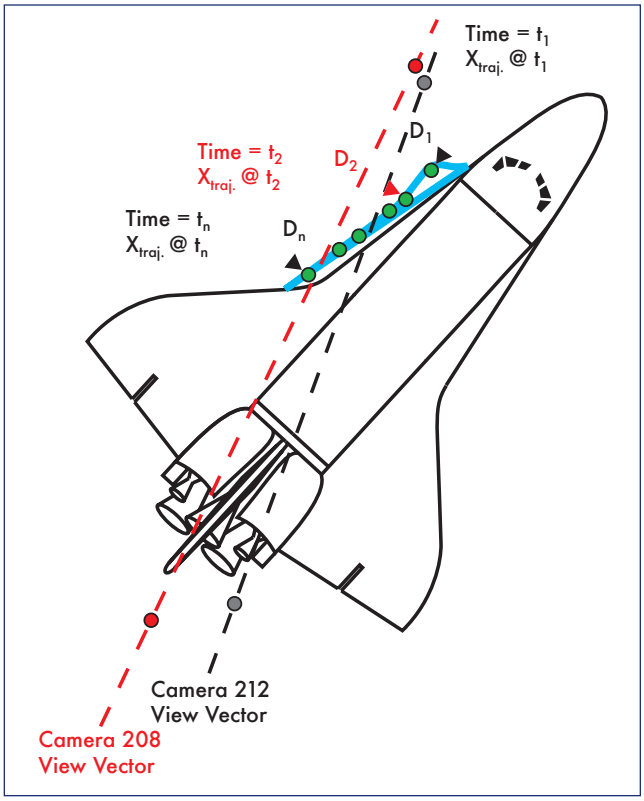

Figure 7-8. Illustration of time-dependent position differences between view vectors for ground cameras 208 and 212 and an integrated trajectory (solid curve) employing a flight-based local velocity flow field. The objective (minimized) function is the sum of the squares of the distances between some or all eleven of these time-dependent position points (ΣD_n^2).

The minimization of the sum square error between the integrated trajectories and the camera (208 and 212) view vectors was confined to these regions. Propagation of the state vector was performed using the position dependent local velocity data grid provided by JSC/EG3 (as used for part 1). In addition to the data associated with the index interval endpoints (i.e., 7-13, 7-16, 8-13, and 8-16), BN, projected impact velocity, projected impact time, and sum square error were

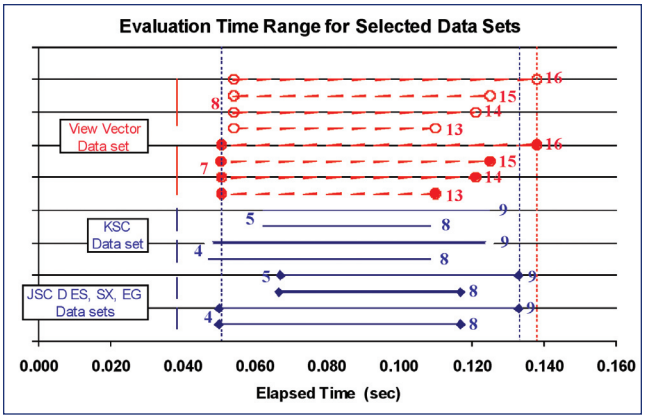

Figure 7-9. The index intervals for the comparison of an integrated trajectory with the view vectors from cameras 208 and 212 are designed to provide similarity to the intervals using in the reference data set comparisons in the previous section. The index ranges used to generate the most probable estimates of key parameters (BN, projected impact velocity, etc.) were 7-13, 7-14, 7-15, 7-16, 8-13, 8-14, 8-15, and 8-16.

evaluated for all internal index point ranges surrounding these endpoints (i.e., 4-8, …, 4-17, 5-9, … , 5-17, … , 13-17). Contour plots of these data are presented in Appendix C.

7.1.5 Observations

The contour plots for BN, projected impact velocity (at X = 1817.45 inches), projected impact time and sum square error (Appendix E3) encompass the index range of interest (7-13, 7-16, 8-13, and 8-16). This index range was the focus for generating the parameters of interest (BN, projected impact velocity, projected impact time). The data in this index range of interest are relatively consistent and homogeneous, given the sparseness and the uncertainty of the image-based comparison data (view vector data). The contour plots show the significant sensitivity of these parameters to the start and stop index values, and appear to reinforce the jittery nature of this sparse data.

Several different trajectory optimization approaches were employed. All impact velocity and time computations were projected to X = 1817.45 inches. The data in figures 6-10(a, b, and c) show the BN, projected impact velocity, and projected impact time for these optimization approaches. The first bar (left most – lightest) in each plot shows the results based on the original MSFC data. Note point 14 (index 7-14 and 8-14) shows a large excursion in the parameters. It is particularly apparent for BN in Figure 7-10. The second plot bars reflect an adjustment to the time stamp of camera 208, which is moved up (earlier) by 6.75 milliseconds. This adjustment was based on feedback from MSFC that it produced the best imaging data results. Again, some excursion in the data can still be seen for point 14. A conversation with MSFC personnel revealed that MSFC had trouble with this particular frame (index) due to image blur. It appears that the trajectory results performed at JSC reflected the uncertainty in the view vector data for index 14. Subsequently, the author performed another trajectory optimization with the data for index 14 removed (3rd more heavily shaded bar). The result was data that appeared to be much more consistent. Finally, the camera view vector errors were used in the computation of the objective function (sum square

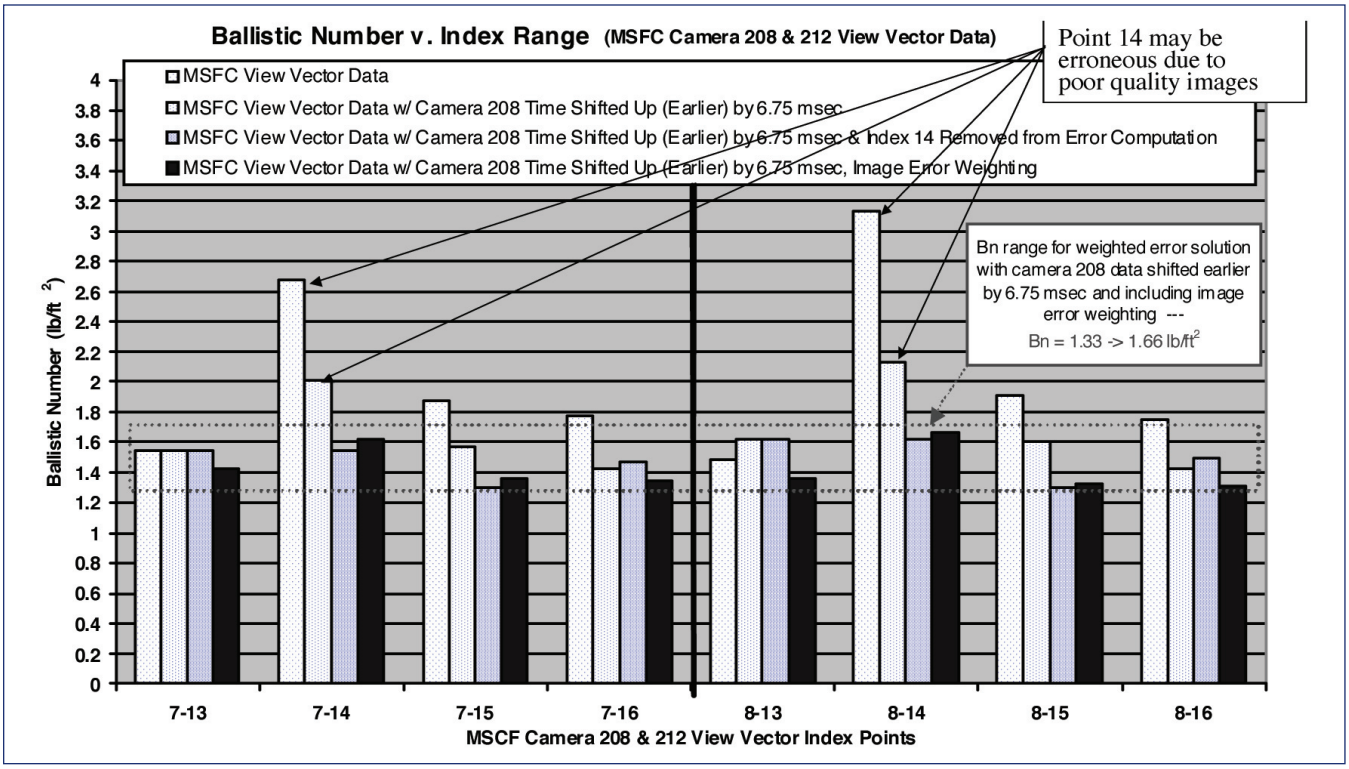

Figure 7-10. BN vs. index range for selected view vector data comparisons.

				Controls							Objective Function (Min)			
				Initial State						Initial Bn				
Data Set	Intervals	Initial Interval Time	Final Interval Time	X	Y	Z	Vx	Vy	Vz	Ballistic Number	Sum Square Position Error	Average Error per Interval	Projected Velocity @ X = 1817 in.	Projected Impact Time @ X = 1817 in.
		(sec)	(sec)	(in)	(in)	(in)	(fps)	(fps)	(fps)	(lb/ft^2)	(in^2)	(in^2)	(fps)	(sec)
View Vector	7-13	0.04975	0.110	1135.01	-116.45	578.63	81.93	-58.87	55.02	1.426	55	9	796	0.164
View Vector	7-14	0.04975	0.121	1134.17	-116.51	578.76	84.74	-50.61	52.06	1.620	100	14	759	0.170
View Vector	7-15	0.04975	0.125	1137.172	-117.017	579.1242	28.31112	-43.0193	50.10038	1.360	203	25	804	0.166
View Vector	7-16	0.04975	0.138	1136.68	-116.73	579.04	31.15	-45.30	50.77	1.345	208	23	808	0.166
View Vector	8-13	0.05000	0.110	1141.65	-120.80	576.02	120.18	-71.90	66.79	1.353	36	7	814	0.162
View Vector	8-14	0.05000	0.121	1146.41	-124.49	577.01	69.49	-34.24	56.23	1.661	81	14	742	0.172
View Vector	8-15	0.05000	0.125	1143.63	-119.87	577.65	14.74	-38.24	53.23	1.328	199	28	807	0.166
View Vector	8-16	0.05000	0.138	1143.24	-119.50	577.56	15.44	-40.07	53.77	1.314	203	25	811	0.166

Table 7-3. BN and projected impact velocity and time (at X = 1817.45 inches) results for comparison of minimum sum square error between ground camera (208 & 212) view vectors and the integrated trajectory. This data is based on movement of the time stamp for camera 208 earlier by 6.75 milliseconds and includes view vector location errors in computation of the sum square perpendicular error between the integrated trajectory and the view vectors at a succession of index points.

error) to produce a weighted error trajectory comparison to the view vector data (right most solid bar). While this data did include index 14, it appeared to be relatively consistent. This last data set was selected as the most representative of the actual foam debris flight characteristics, given the data available.

Table 7-3 shows a summary of the BN values along with the projected impact velocity and time at X = 1817.45 inches. The table shows the 7 controls used in the trajectory optimization including the initial state and the BN. The optimization minimized the objective function or the sum square perpendicular distance error between the integrated trajectory and the view vectors at successive index points.

For the index intervals evaluated, the resulting BN ranged from 1.314 to 1.661 $lb./ft^2$ and the projected impact velocity of the foam debris at X-position of 1817.45 inches ranged from 742 to 814 fps.

The foam debris trajectories for index ranges (7-13, 7-14, 7-15, 7-16, 8-13, 8-14, 8-15, and 8-16) are depicted in an oblique view of the Shuttle (Figure 7-13). These trajectories represent the optimal selection of the initial state and a constant BN to provide a minimum sum square error over the selected index interval. They begin at the initial state and are projected to impact the left Shuttle wing*. For all cases the debris impacts the Shuttle on Reinforced Carbon-Carbon (RCC) panels 7, 8, or 9.

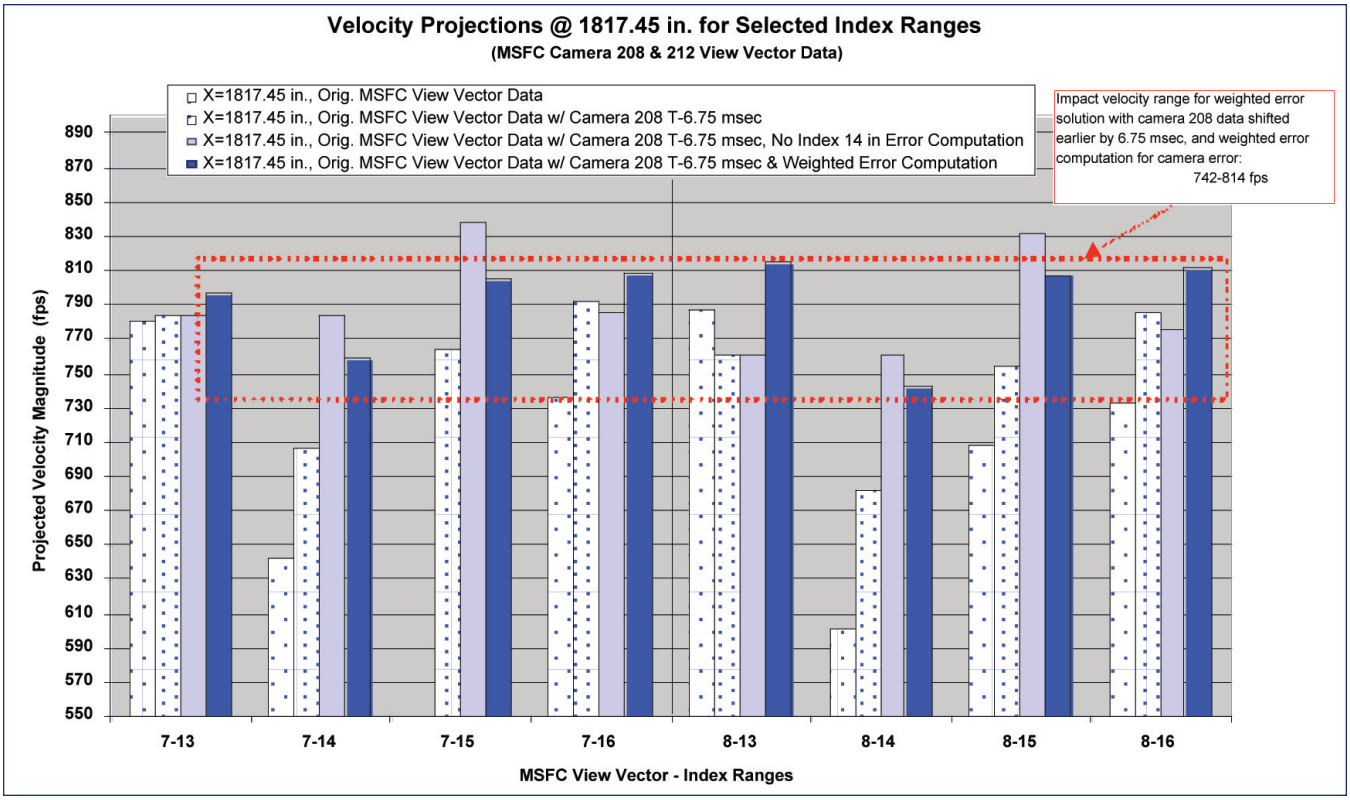

Figure 7-11. Projected impact velocity at X-position = 1817.45 inches vs. index range for selected view vector data comparisons.

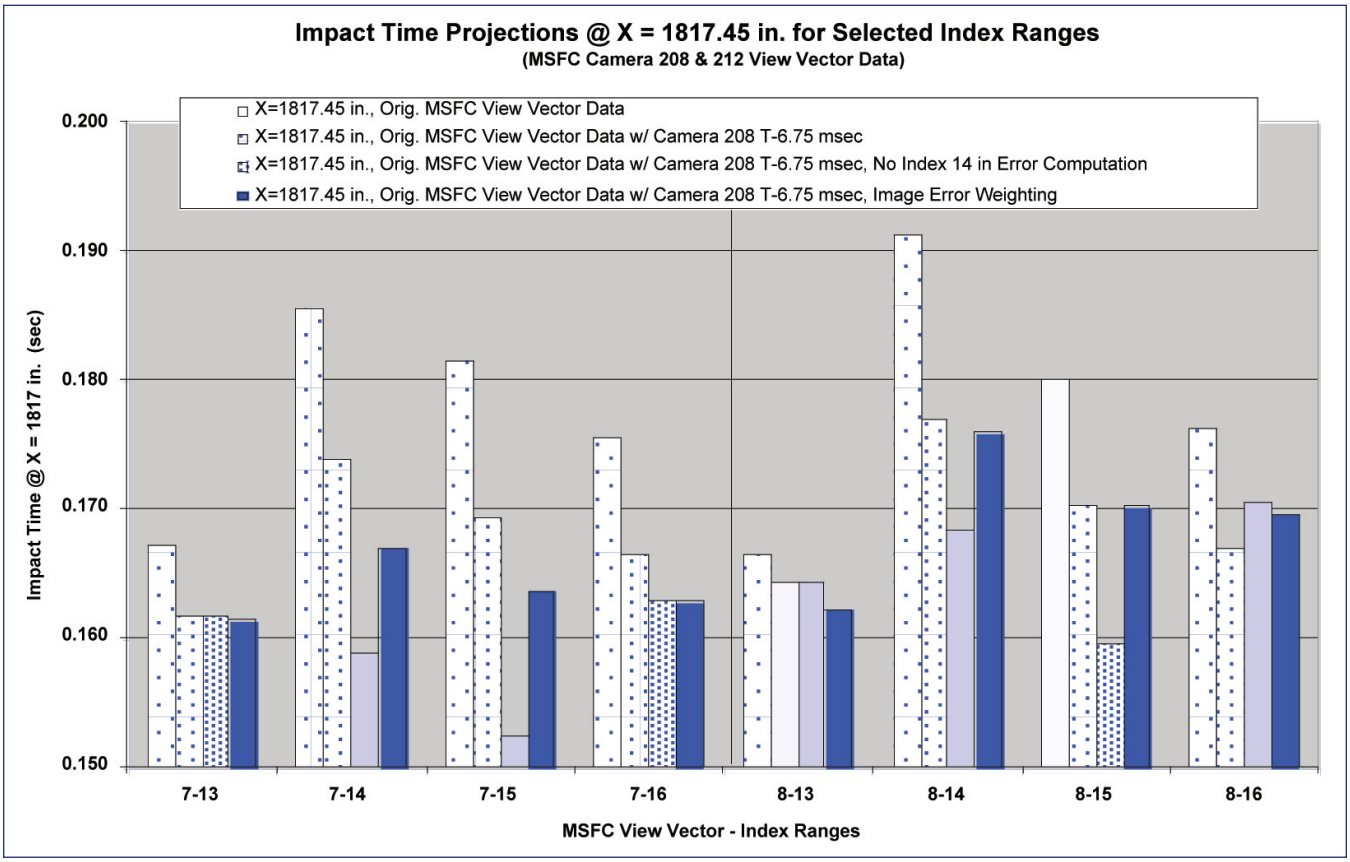

Figure 7-12. Projected time of impact at X-position = 1817.45 inches vs. index range for selected view vector data comparisons.

An enhanced view of the impact locations (Figure 7-12) shows the projected impact locations on the leading edge of the Shuttle wing. While all eight selected index interval trajectories were projected to hit the wing, several appeared to hit high on the wing leading edge (trajectories 8-13 and 8-14, possibly 7-13 and 7-14). Imagery data showing debris emerging from under the wing suggest a debris impact on the lower leading edge. A grouping of four trajectories (7-15, 7-16, 8-15, 8-16) appears on RCC panels 7 & 8 on the lower leading edge. A top view of the Shuttle with these trajectories shows that the impacts occurred with an outboard angle to the trajectory (see Figure 7-14).

The impact velocities for the selected-index-intervals trajectories shown in Figures 7-10 through 7-12 range from 729-815 fps, with the bulk of the velocity component in the ET coordinate frame x-direction (see Table 7-4). The trajectory heading ranges from about 6.5°-7.5° outboard at impact

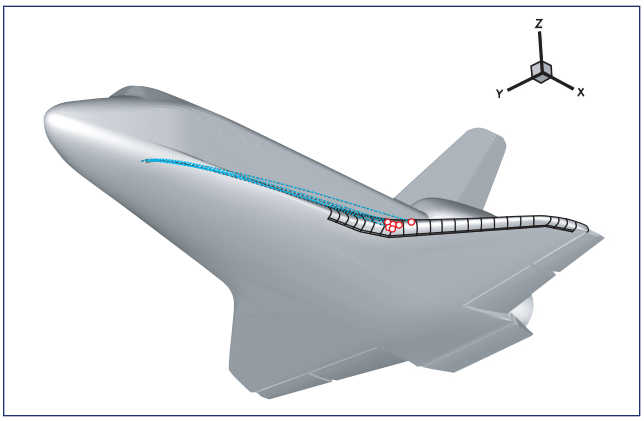

Figure 7-13. Optimized foam debris trajectories for index intervals 7-13, 7-14, 7-15, 7-16, 8-13, 8-14, 8-15, and 8-16, projected to Shuttle impact. Graphic courtesy of Phil Stuart – JSC/EG3.

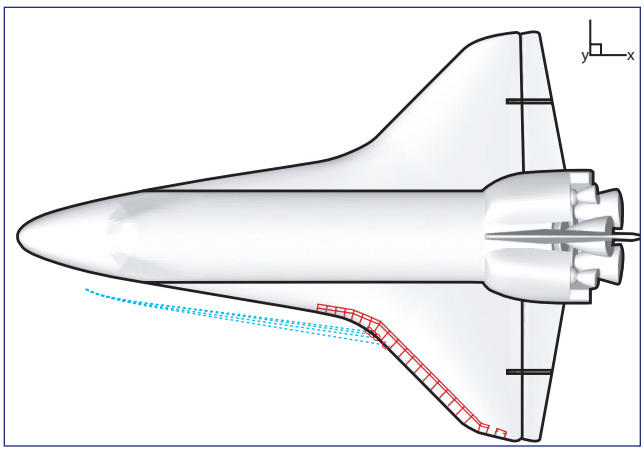

Figure 7-14. Top view of optimized foam debris trajectories for index intervals 7-13, 7-14, 7-15, 7-16, 8-13, 8-14, 8-15, and 8-16, projected to Shuttle impact and showing outboard direction of trajectory at impact. Graphic courtesy of Phil Stuart – JSC/EG3.

								Impact angle - relative to Shuttle wing			
	Impact Position			Impact Velocity					Trajectory heading - relative to E.T. coordinate frame		
Index Interval	X (inches)	Y (inches)	Z (inches)	Vx (fps)	Vy (fps)	Vz (fps)	Vmag (fps)	Impact Angle (deg)	Angle X-Y (deg)	Angle X-Z (deg)	Angle Y-Z (deg)
7-13	1806.63	-231.14	630.24	784.98	-98.77	28.45	791.68	31.83	2.03	-7.16	82.56
7-14	1796.85	-223.44	630.41	743.94	-91.00	27.65	750.00	29.89	2.13	-6.97	82.71
7-15	1797.70	-217.53	624.55	789.94	-91.46	22.37	795.53	15.46	1.62	-6.60	83.20
7-16	1799.12	-219.39	624.94	794.44	-93.00	22.93	800.20	15.81	1.63	-6.67	83.14
8-13	1827.05	-247.37	637.56	807.41	-107.57	36.85	815.37	29.55	2.59	-7.58	81.98
8-14	1786.80	-215.39	633.33	724.08	-81.86	30.30	729.32	26.08	2.40	-6.44	83.12
8-15	1792.08	-215.63	625.54	790.12	-89.63	23.81	795.54	15.79	1.70	-6.47	83.31
8-16	1793.51	-217.01	625.78	794.47	-90.90	24.18	800.02	16.94	1.71	-6.53	83.25

Table 7-4. Foam debris data for selected index interval trajectories impacting the Shuttle wing as depicted in Fgures 6-11, 6-12, and 6-13.

(as shown in Figure 7-15). The trajectory angle between the incoming debris trajectory and the Shuttle wing leading edge (impact angle) has a range of about 15.5°-31.8°. For all cases, the impacting debris trajectory lies within about 2.5° of the z-plane (angle x-y).

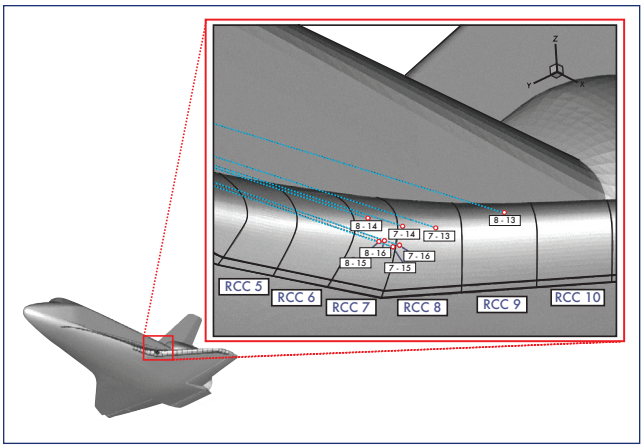

Figure 7-15. Close-up of optimized foam debris trajectories for index intervals 7-13, 7-14, 7-15, 7-16, 8-13, 8-14, 8-15, and 8-16, projected to Shuttle impact. Graphic courtesy of Phil Stuart – JSC/EG3.

7.1.6 Conclusions

The reference data sets (JSC/ES, JSC/SX, KSC, and JSC/EG) and the MSFC view vector data sets provided sparse and choppy sources on which to generate position, velocity, and BN estimates for the foam debris that impacted the Shuttle's left wing. That being said, part 1 of this portion of the trajectory analysis (i.e., comparison to the above-mentioned reference data sets) favored the KSC data as producing the most consistent results. For this part, the BN ranges from 1.23-1.45 lb/ft^2 with an estimated range of impact velocities between 763 and 803 fps (at an X-position of 1800 in.). The author feels, however, that the trajectory comparisons were better served by the MSFC view vector data. This is because view vector data possessed more of a raw measurement characteristic than the pre-processed (approximated, curve fit) data, as shown in part 2. For this case, the integrated trajectories were propagated, in a local velocity flow field, to impact on the Shuttle's left wing. For these minimum sum square error trajectory integration comparisons with the view vector data, the average BN for a selected index interval (shown in Table 7-3) ranges from 1.314 to 1.661 lb/ft^2 with a Shuttle impact velocity magnitude range of 729.3 to 815.4 fps.

7.2 Lee Analysis: Least Squares Optimized with View Vector Data

This study was an attempt to model the motion of the large debris object that apparently separated from the STS-107 external tank at approximately 81.7 seconds MET and subsequently impacted the left wing of the Orbiter. This analysis used image analysis observations together with dynamics models and realistic flow fields to estimate the most likely trajectory of the debris object. The study determined "best fit" debris trajectories including approximate impact velocities, and developed information on the aerodynamic properties of the object, which could be used to infer the likely mass of the debris object.

7.2.1 Approach & Methodology Trajectory vs. Pre-processed Imagery Data Sets

The approach was to find the most likely trajectory of the debris object by fitting the trajectory to observational data from image analysis. The motion of the debris object was modeled using dynamics equations and Runge-Kutta type numerical integrators. The initial conditions and aerodynamic parameters were selected to provide the closest fit between the debris object motion and the image analysis observations, according to an uncertainty-weighted least squares fit approach. An elementary trial-and-error optimization routine was used to seek the initial conditions and aerodynamic parameters for the best fit trajectory.

The objectives were:

1. To develop an estimate of the ballistic number (BN) of the debris object. The ballistic number, which is the weight divided by the product of the coefficient of drag and the corresponding reference area, determines the relative effect of drag versus momentum. For an object primarily influenced by drag, it is the key aerodynamic parameter. Together with knowledge about the material density and approximate shape of the object, the ballistic number could be used to infer an approximate mass.
2. Estimate the impact velocity of the debris.
3. Model the path of the debris to estimate impact location and impact angle.

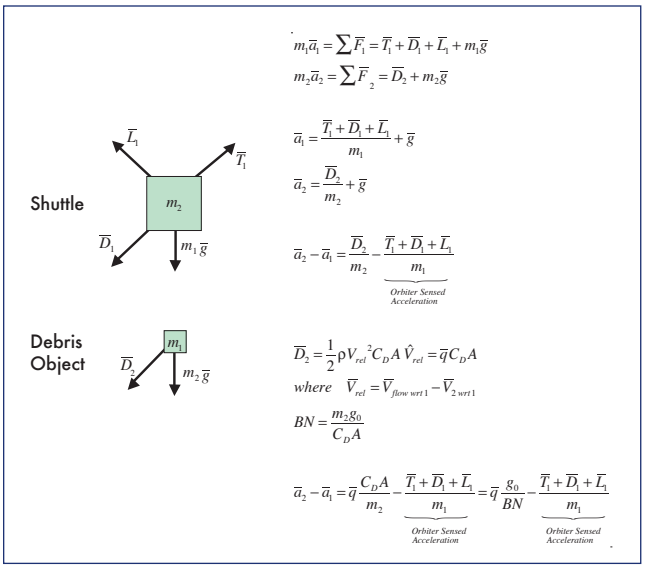

Figure 7-16. Ballistic equations of motion for debris object relative to the Space Shuttle.

Figure 7-16 presents a brief derivation of the equations of motion. This derivation is for a "ballistic" model – That is it includes drag, but no lift force on the debris object. The subscript 1 indicates the STS; subscript 2 indicates the debris object. Overbars indicate vectors, and "hats", or bent bars indicate unit vectors. In general, vector names are as follows:

m – Mass
a – Acceleration
g – The local acceleration due to gravity
g_0 – The sea-level-standard value of the acceleration of gravity
F – Force
T – Thrust
L – Lift
D – Drag
V – Velocity
ρ – Local air flow density
C_D – Coefficient of drag for the debris object
A – Reference area for the C_D
BN – Ballistic number

The final result is the equation for the relative acceleration of the debris object with respect to the STS. This is the equation evaluated in the Runge-Kutta propagation routines. Note that for cases such as this where the STS and the debris object are in close proximity, the local gravitational acceleration cancels out of the relative acceleration equation. Note also how much simplified the equation becomes when the ballistic number term is used – this makes solution for an unknown object much more feasible.

A realistic flow field about the STS was used in calculating the drag force. This flow data was developed using computer models and supplied by Ray Gomez and Darby Vicker of the JSC EG3/Applied Aeroscience and CFD branch. The flow data included velocity components, local air density, and local speed of sound. It was provided in a ten inch grid referenced to STS External Tank structural coordinates, i.e. data points spaced by ten inches in each direction, over the region of interest.

The image analysis data we used was in the form of "view vectors", or "view lines". At first, we were using three-dimensional points derived by the various image analysis groups as the basis for our trajectory fitting approach. However, we decided that the view lines developed by the image analysis groups gave us a better basis for our trajectory estimates. Only the vector-based results will be presented in this section.

Each image, in which the debris object is visible, gives us a line from the camera through the debris object. A single image can't give us a three-dimensional position in this case. And though some are very close, no two images occur at exactly the same time. (Even if they did, observational uncertainties would mean that the view lines don't necessarily pass through the same point in space.) In developing the "imagery only" three-dimensional position estimates, the image analysts had to make assumptions, which were probably geometrically based.

Complicating matters, the angle between the camera views, measured at the Orbiter, was fairly small (only 17.3 degrees). This means a little uncertainty in one view can "stretch out", making a large uncertainty along the view direction. (See Figure 7-17- but note that the situation with simultaneous intersecting view lines is for illustration only.)

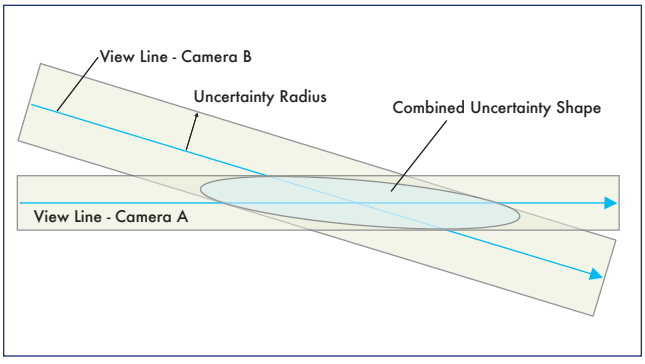

Figure 7-17. Combined uncertainty shape for camera views with small intersection angle.

Using the view lines allows us to take into account the actual shape of the "uncertainty corridor". It allows us to "lace" the observation data together using a physical model of the motion.

The times of the observations also presented challenges. Some image analysis experts felt that the time stamp from the video imagery was not reliable. Also, truncation errors were obvious in both sets of the observation time stamps.

However, the frame rates of the cameras were known with very good precision. In order to develop better estimates of relative observation times, the camera frame rates were used to establish intervals between observations for each camera respectively. The time offset between the first observations from each of the two cameras was then determined as an output of the optimization routine.

In terms of aerodynamic forces, most of this study modeled only the drag force. However, limited work was done to model lift. A rotating disk model was employed, assuming a constant rotational rate and direction. Attempting even a simple model of lift involves fitting several more parameters, and in general, it was felt that there was not enough observational data to resolve the lift properties of the object. Also, convergence times were very long for the optimization routine with the lift model, and schedule constraints made an extensive examination impossible. However, with these caveats, some limited results of the lift model will be discussed in this report.

The orbiter sensed acceleration components used in the simulation, expressed in the STS External Tank structural coordinate frame, were:

Ax = -75.163 ft/s^2
Ay = -0.058 ft/s^2
Az = -2.472 ft/s^2

These values were assumed not to change significantly over the less than 0.2 second transit time of the debris object.

Also, the attitude of the STS was assumed not to change significantly over the time period of the simulation.

7.2.2 Input Data from Image Analysis – View Vectors

Observational data in the form of three-dimensional points was received from image analysis teams at MSFC, KSC, and the SX, ES, and EG divisions of JSC. The view vector form of the data was requested later as analysis methods were developed. Due to time limitations, only the MSFC view vector data was analyzed, and it forms the basis for the analysis presented here.

View vector/line sets were obtained for two cameras: E-212 and ET-208. Info from image analysis is summarized as follows:

E-212 is a film camera with a frame rate of 64 frames per second. The view is from over the wing and aft. It renders the closest and clearest view of the debris transit, but the object is obscured by the Orbiter wing in this view before impact. This camera renders 10 frames of visibility for the debris transit, the last only partial. Image analysis experts give an uncertainty radius for view vectors from this camera of about 8 or 9 inches.

ET-208 is a video camera, and it operates at 60 frames per second. The view is looking under the wing from a position somewhat aft. This view is farther away and the images are somewhat fuzzier, but the object is visible all the way to impact (and past). There are again 10 frames from this camera during the transit of the debris object, but only 7 or 8 frames have a clearly resolvable image of the object. The estimated uncertainty radius for view vector observations from this camera is in the range of 20 to 30 inches.

From camera E-212, view vector observations 1 though 9 were used in this analysis (corresponding to frames 4913 to 4921). The tenth view vector (from frame 4922) was discarded, as it was based only on a view of the edge of the object, with the bulk hidden behind the wing.

From the video camera ET-208, view vectors corresponding to frames 1 to 5, and 9 and 10 of the debris transit were used. No view vectors were used corresponding to frames 6, 7, or 8: The object is not clearly visible in frames 6 and 7. Frame 8 also has very marginal visibility, and this view vector appears to be inconsistent with other view vectors, as noted by Condon. MSFC also presented a view vector corresponding to frame 11 from this camera, but it represents the post-impact debris cloud and was not used in this analysis.

7.2.3 Results

Several ballistic cases were examined, using different start times and therefore including different subsets of the view vectors. (i.e. later start times would exclude the earlier view vectors.) This approach was taken in case the later segment could be better approximated with a ballistic (i.e. non-lifting) model.

The flow field data was provided in a 10 inch grid. This seemed sufficient for most of the flow field. However, interpolation of the flow data required that we start our trajectory calculations an adequate distance away from STS structure, since flow interpolation wasn't accurate if a "buried" grid point was included. Also, flow gradients were largest directly next to structure. This set an effective limit on the start time for our trajectory simulations – the net effect was that the first view vector for each camera could not be included in the solution.

For several of the cases, the best fit-solution included a negative X velocity in the ET coordinate frame (that is the debris object is moving forward at the beginning of the simulated time interval). While the complex aerodynamic forces involved in the separation of the debris object from the bipod ramp region might provide some justification for such a result very early in the trajectory, negative initial X-velocities for simulations starting later in the trajectory suggest spurious solutions. The reasons for these spurious solutions could

have to do with sparsity of data and data noise, and/or with the assumptions of a constant coefficient of drag and no lift.

The most reliable ballistic trajectory solution was selected by eliminating several of these spurious solutions, and using the general rule of thumb that a solution including more observational data is better. The solution selected is one with a start time of 0.014 sec after the first E-212 camera frame. This is depicted in figures 6-16 and 6-17. It includes all of the selected view vector data except the first vector from each camera (as discussed).

Impact velocity is between about 800 and 820 ft/s depending on where contact occurs. The estimated ballistic number is 1.397. The debris object mass center passes close beneath RCC panels 8 and 9 – For an actual finite-sized debris object the initial impact for this trajectory would probably be on these panels. The optimization routine calculated a time shift of -4.127 milliseconds for the ET-208 view vector times (i.e. the first ET-208 frame would occur 0.127 milliseconds before the first E-212 frame).

This trajectory solution fits the view vector data pretty well. The trajectory position and time matches are within 8.51 inches of all view vectors, and the average "miss distance" is only 4.73 inches.

It is worth noting, however, that looking at Figure 7-19 ballistic-model trajectories do not seem to originate from an initial position and direction of motion consistent with departure from the bipod ramp location (pretty close, but not quite). Also, looking at Figure 7-18, while the ballistic model can fit the observational data pretty well, it doesn't seem to follow apparent trends in the Z direction. These discrepancies seem to suggest that lift is a significant factor in the trajectory shape.

Modeling a lifting object is much more complex than an object with constant drag, however. Solving for the motion of an object with constant drag involves fitting only a single parameter – the ballistic number. Determining the aerodynamic and rotational properties of a rotating object with lift is significantly more complex.

In general, the number, quality, and arrangement of observations for the STS-107 ascent debris object were not sufficient to fit a model including aerodynamic lift with any confidence. Also, trajectory solutions using a lift model proved to have very long convergence times using the current rather primitive optimization scheme – schedule limitations prevented a more thorough examination. However, some preliminary modeling was attempted. A simplified "rotating disk" model was employed, with a constant rotation rate and an axis of rotation in the plane of the disk.

A single result is presented for comparison: This solution was selected because it had an impact location approximately matching the location suggested by forensic analysis. The object path in this case fits the observational data somewhat better than the ballistic solution – particularly in the Z-axis direction. It may be a better approximation of the actual object motion. This case was constrained to have a rotation rate

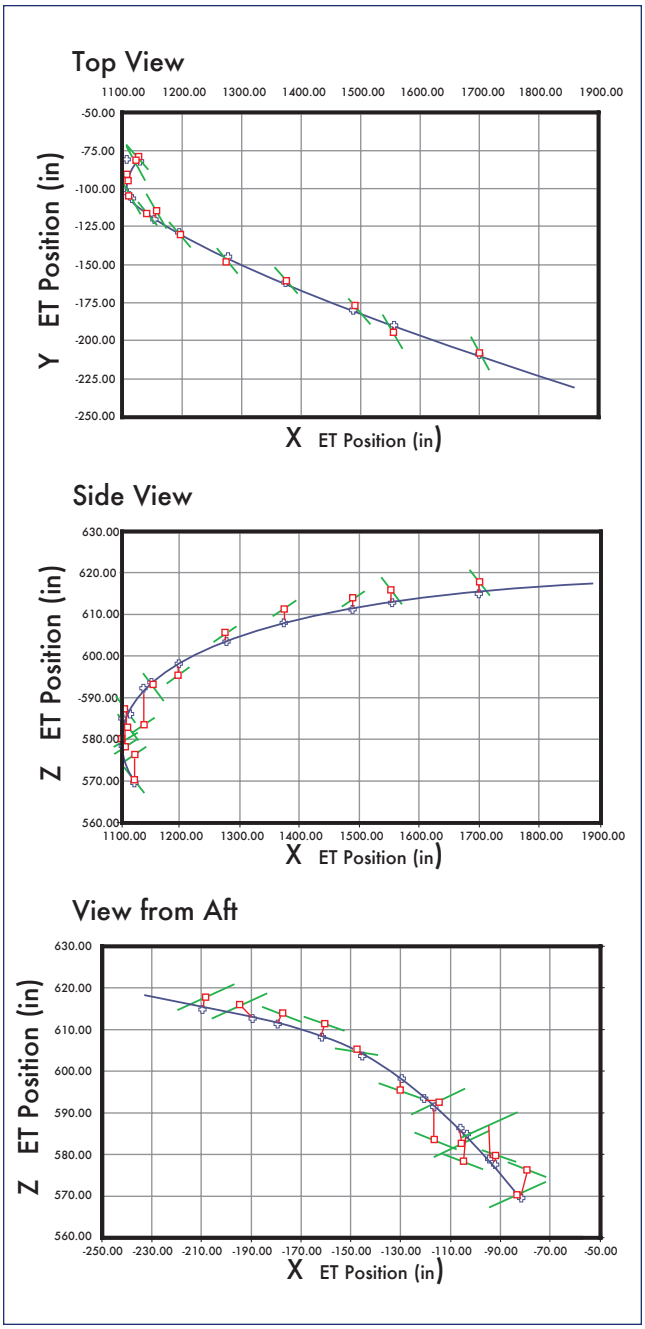

Figure 7-18. Debris object trajectory solution with view vectors (ballistic model).

of 5 rotations per second – much less than the 18 rotations per second result of the color ratio analysis by Svendsen and Salacin of NIMA.

Details of this lift-based trajectory will not be presented because of its preliminary nature, but for purposes of comparison, the impact velocity is presented. The impact velocity for this solution was approximately 760 ft/s, somewhat lower than the ballistic solution. There are several possible reasons for the solution with lift to have a lower impact velocity than the ballistic model. This particular lifting solution had an impact location slightly forward of the impact location for the

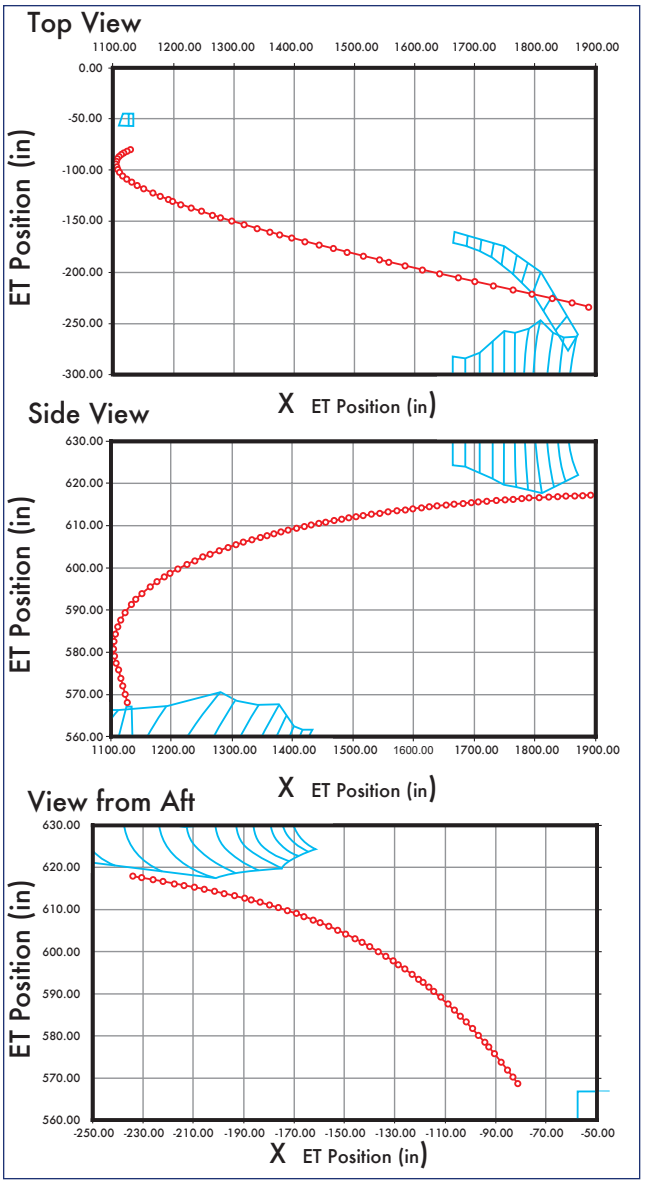

Figure 7-19. Debris object trajectory solution with rcc and bipod ramp outlines (ballistic model).

ballistic model, which means a slightly shorter distance in the flow direction for the debris object to accelerate. The lifting solution has a slightly different path – it travels through different flow regions than the ballistic solution. And the effect of lift and time-varying aerodynamic properties may be that the optimal fit of the motion to the observational data may call for a higher average ballistic number.

7.2.4 Conclusions

Conclusions of the analysis are as follows:

1. Impact location: The ballistic model predicts an impact location in the region of RCC panels 8 and 9.
2. Impact velocity: The ballistic model predicts an impact velocity of approximately 800 to 820 ft/s. A preliminary result of a simplified model including lift predicts an impact velocity of approximately 760 ft/s.
3. The ballistic model estimates a ballistic number of approximately 1.4.
4. Comparison of view vectors with ballistic model trajectory suggests lift was a significant factor in debris motion. However, the number, quality, and arrangement of observations were not really sufficient to fit a model including aerodynamic lift with any confidence.

7.3 Crain Analysis: Batch Least Squares Method with Pre-processed Data

The preprocessed foam position data sets JSC/EG, JSC/ES, JSC/SX, and KSC were also processed in a batch least squares epoch state estimator to refine estimates of the initial foam position, velocity, and ballistic number. This approach refines the initial conditions of the foam debris trajectory (including ballistic number) by minimizing the sum of the squares of the residuals between the predicted foam debris locations, developed by propagating through a Space Shuttle flow field model, and the observed locations (from the image analysis data sets). This process is widely used to reduce data in the scientific community and has the advantage of providing a statistical confidence of the initial conditions that is a function of the assumed measurement accuracy and the system dynamics. A qualitative illustration of this process is provided in Figure 1 and the formulation of this approach is easily obtained from the mathematical and statistical literature.

The specific goal of this approach was to quantify the average ballistic number that best fit the available camera data of the foam debris trajectory. This ballistic number would be accompanied by a batch least squares statistical confidence number derived from the initial estimate covariance produced by the least squares algorithm. Following the lead of the other approaches, not all of the available data was processed together. In fact, varying start and stop points in the data were used to investigate the sensitivity of foam debris passing through different observational or dynamical

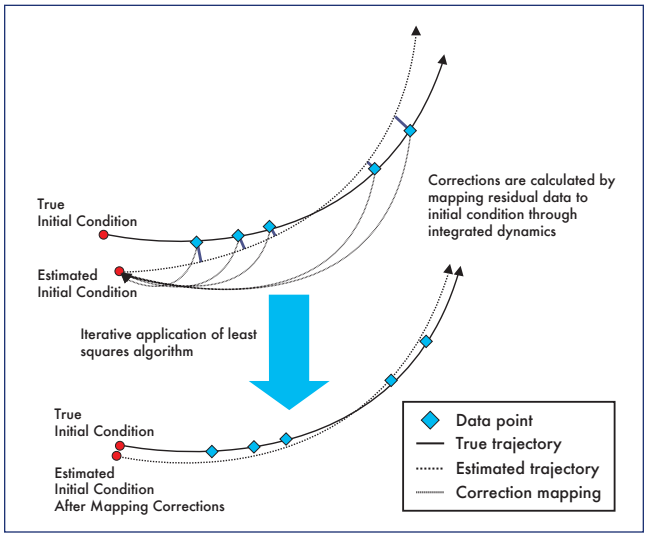

Figure 7-20 Batch least squares estimation process.

regimes of the Space Shuttle vicinity. The initial ballistic number estimates and the 1–σ confidence intervals on these estimates are provided in Table 6-5. The columns within each data set represent final data values while rows characterize initial data values. For example, the EG BN estimate of 1.15 occurs at the 3 row and 7 column indicating that the estimate was obtained from least squares processing of EG data points 3, 4, 5, 6, and 7. The measurement accuracy of each foam debris data point in each preprocessed data set was considered to be 8.0 inches in all three coordinates.

Generally, ballistic number confidences were higher when more data was processed (resulting in smaller 1-sigma values in the '10' column of each data set). The JSC/SX data set had the smallest overall statistical confidence values indicating a higher probability that the ballistic numbers, for most of the available data, were more representative of the foam debris data as compared to other data sets.

EG Data BLS Bn Estimate

From V, To->	7	8	9	10
1				
2				
3	1.15	1.33	1.66	1.82
4	1.01	1.41	2.15	2.29
5		1.21	2.54	2.61
6				

EG Data BLS Bn 1-sigma

From V, To->	7	8	9	10
1				
2				
3	0.12	0.12	0.14	0.13
4	0.20	0.25	0.38	0.31
5	0.00	0.30	0.79	0.57
6				

ES Data BLS Bn Estimate

From V, To->	7	8	9	10
1				
2				
3	3.57	2.14	1.83	1.90
4	0.00	2.48	1.79	1.92
5	0.00	0.00	1.08	1.43
6				

ES Data BLS Bn 1-sigma

From V, To->	7	8	9	10
1				
2				
3	1.55	0.37	0.20	0.16
4	0.00	0.88	0.31	0.26
5	0.00	0.00	0.19	0.23
6				

KSC Data BLS Bn Estimate

From V, To->	7	8	9	10
1				
2				
3	1.87	1.71	1.65	1.65
4	1.35	1.41	1.45	1.52
5	0.00	1.24	1.40	1.53
6				

KSC Data BLS Bn 1-sigma

From V, To->	7	8	9	10
1				
2				
3	0.51	0.28	0.18	0.14
4	0.54	0.33	0.23	0.18
5	0.00	0.51	0.38	0.30
6				

SX Data BLS Bn Estimate

From V, To->	7	8	9	10
1				
2				
3	4.00	1.87	1.65	1.61
4	2.42	1.21	1.21	1.31
5	0.00	0.89	1.03	1.24
6				

SX Data BLS Bn 1-sigma

From V, To->	7	8	9	10
1				
2				
3	1.98	0.29	0.16	0.12
4	1.42	0.21	0.14	0.12
5	0.00	0.23	0.19	0.18
6				

Table 7-5 (above). Batch Least Squares Estimates and Confidences for Initial BN by Data Set.
Table 7-6 (below). Batch Least Squares Estimation Error and Average Interval Estimation Error Table.

EG Data BLS Sum Square Error (in.^2)

From V, To->	7	8	9	10
1				
2				
3	909	1,240	2,313	2,580
4	859	1,216	1,861	1,898
5	0	1,159	1,805	1,816
6				

EG Data BLS Sum Squared Error per Interval (in.^2)

From V, To->	7	8	9	10
1				
2				
3	227	248	385	369
4	286	304	372	316
5	0	386	451	363
6				

ES Data BLS Sum Square Error (in.^2)

From V, To->	7	8	9	10
1				
2				
3	952	1,713	2,209	2,717
4	0	1,208	1,526	1,760
5	0	0	345	716
6				

ES Data BLS Sum Squared Error per Interval (in.^2)

From V, To->	7	8	9	10
1				
2				
3	238	343	368	388
4	0	302	305	293
5	0	0	86	143
6				

KSC Data BLS Sum Square Error (in.^2)

From V, To->	7	8	9	10
1				
2				
3	194	264	321	425
4	57	68	109	186
5	0	47	105	176
6				

KSC Data BLS Sum Squared Error per Interval (in.^2)

From V, To->	7	8	9	10
1				
2				
3	48	53	54	61
4	19	17	22	31
5	0	16	26	35
6				

SX Data BLS Sum Square Error (in.^2)

From V, To->	7	8	9	10
1				
2				
3	965	1,882	2,066	2,093
4	56	624	726	826
5	0	452	560	727
6				

SX Data BLS Sum Squared Error per Interval (in.^2)

From V, To->	7	8	9	10
1				
2				
3	241	376	344	299
4	19	156	145	138
5	0	151	140	145
6				

The summed estimation error for each data set processed is presented in Table 7-6. The KSC data had the best final fit to the least squares solution followed by the JSC/SX data set. This result tends to support the deterministic results of Condon and Lee. The JSC/EG and JSC/ES data were comparable to each other in their final fit to the least squares solution; however, the ES data did not converge to a solution in the cases of ES4-7 (starting with the 4th data point and ending with the 7th) and ES5-8 (starting with the 5th data point and ending with the 8th).

The ballistic numbers of the JSC/EG, JSC/SX, and KSC data sets were fused into a weighted average based upon their statistical confidence levels as presented in Table 7-7. This approach provides the most representative ballistic number of all of the data from these preprocessed data sets

	IMPACT CHARACTERISTICS										
DATA	x in	y in	z in	u ft/s	v ft/s	w ft/s	vel ft/s	ang deg	angxy deg	angxz deg	angyz deg
EG3-7	1823.3	-209.2	617.5	849.1	-92.6	10.8	**854.2**	5.1	0.7	-6.2	83.8
EG3-8	1815.7	-212.4	619.0	803.9	-90.7	13.7	**809.1**	8.0	0.9	-6.4	83.5
EG3-9	1808.6	-215.0	620.9	737.3	-86.7	16.6	**742.6**	10.9	1.3	-6.7	83.2
EG3-10	1807.5	-217.3	621.8	714.1	-86.3	17.8	**719.5**	11.8	1.4	-6.9	82.9
EG4-7	1822.3	-208.5	617.4	885.3	-95.2	10.6	**890.5**	5.2	0.7	-6.2	83.8
EG4-8	1809.4	-212.4	620.1	785.7	-89.9	16.0	**791.0**	8.9	1.2	-6.5	83.4
EG4-9	1802.7	-215.4	622.4	688.3	-84.3	19.6	**693.7**	11.5	1.6	-7.0	82.9
EG4-10	1804.8	-217.7	622.6	677.7	-85.1	19.9	**683.3**	12.5	1.7	-7.2	82.7
EG5-8	1813.5	-212.8	619.5	820.5	-93.1	14.6	**825.9**	8.9	1.0	-6.5	83.4
EG5-9	1802.6	-216.4	622.7	666.8	-84.4	20.1	**672.5**	12.6	1.7	-7.2	82.6
EG5-10	1805.5	-218.6	622.7	663.8	-86.1	20.1	**669.7**	12.5	1.7	-7.4	82.4
ES3-7	DID NOT HIT SURFACE										
ES3-8	1833.5	-252.5	639.1	690.1	-87.0	29.4	**696.2**	28.4	2.4	-7.2	82.4
ES3-9	1812.0	-234.4	635.6	719.0	-81.5	28.2	**724.1**	29.3	2.2	-6.5	83.2
ES3-10	1793.2	-220.1	632.9	699.9	-72.1	26.2	**704.1**	29.5	2.1	-5.9	83.8
ES4-7	LEAST SQUARES SOLUTION DID NOT CONVERGE										
ES4-8	1822.3	-232.3	644.6	653.5	-67.4	35.3	**657.9**	19.7	3.1	-5.9	83.4
ES4-9	1795.7	-219.8	636.8	716.3	-66.4	30.5	**720.0**	25.5	2.4	-5.3	84.2
ES4-10	1777.0	-209.1	633.1	691.3	-57.2	27.1	**694.2**	25.2	2.2	-4.7	84.8
ES5-8	LEAST SQUARES SOLUTION DID NOT CONVERGE										
ES5-9	1772.0	-206.6	631.5	810.8	-57.4	24.0	**813.2**	25.1	1.7	-4.0	85.6
ES5-10	1759.9	-200.1	630.3	733.3	-45.6	22.5	**735.1**	24.3	1.8	-3.6	86.0
KSC3-7	1826.1	-245.9	627.5	710.4	-97.0	21.0	**717.3**	24.3	1.7	-7.8	82.1
KSC3-8	1812.1	-235.8	632.4	725.8	-95.0	25.4	**732.5**	33.8	2.0	-7.5	82.3
KSC3-9	1805.2	-229.3	628.6	731.9	-92.4	22.5	**738.0**	27.6	1.8	-7.2	82.6
KSC3-10	1798.8	-222.7	627.0	728.3	-88.6	21.1	**734.0**	20.7	1.6	-6.9	82.9
KSC4-7	1804.2	-229.1	631.0	781.1	-94.7	26.2	**787.3**	31.7	1.9	-6.9	82.8
KSC4-8	1803.4	-226.4	636.3	767.5	-91.9	30.8	**773.6**	26.8	2.3	-6.8	82.8
KSC4-9	1795.7	-222.5	630.4	755.7	-88.7	25.4	**761.3**	29.6	1.9	-6.7	83.1
KSC4-10	1789.9	-217.4	628.0	741.1	-84.0	23.0	**746.2**	22.1	1.8	-6.4	83.3
KSC5-8	1805.3	-226.1	638.4	798.2	-94.3	34.1	**804.4**	23.9	2.4	-6.7	82.8
KSC5-9	1794.5	-221.6	630.6	763.2	-88.3	25.7	**768.7**	29.6	1.9	-6.6	83.1
KSC5-10	1788.1	-216.0	627.7	739.1	-81.8	22.5	**743.9**	22.2	1.7	-6.3	83.5
SX3-7	DID NOT HIT SURFACE										
SX3-8	1778.6	-204.7	624.3	692.3	-76.5	20.6	**696.8**	13.2	1.7	-6.3	83.5
SX3-9	1785.2	-206.5	623.4	728.6	-80.5	20.0	**733.3**	11.8	1.6	-6.3	83.5
SX3-10	1789.5	-205.9	622.2	736.9	-80.5	18.8	**741.5**	11.2	1.4	-6.2	83.6
SX4-7	1570.7	-148.0	629.7	525.3	-26.3	32.5	**526.9**	8.3	3.6	-2.8	85.4
SX4-8	1730.3	-182.2	624.7	768.8	-64.7	22.4	**771.8**	7.5	1.7	-4.8	84.9
SX4-9	1759.2	-193.8	624.2	785.0	-73.0	21.6	**788.7**	10.7	1.6	-5.3	84.5
SX4-10	1773.0	-198.0	623.0	772.8	-73.9	20.2	**776.6**	10.9	1.5	-5.5	84.3
SX5-8	1739.1	-186.6	625.2	849.7	-76.7	23.0	**853.5**	9.5	1.5	-5.1	84.6
SX5-9	1765.3	-198.1	624.8	824.5	-82.4	22.5	**828.9**	11.4	1.6	-5.7	84.1
SX5-10	1776.9	-201.2	623.3	784.6	-80.3	20.8	**788.9**	10.9	1.5	-5.8	84.0

Table 7-7. Ballistic number estimates and statistical confidences from Fused JSC/EG, JSC/SX, and KSC Data.

Fused Bn Solution from EG/KSC/SX Data

From V, To->	7	8	9	10
1				
2				
3	1.23	1.47	1.66	1.69
4	1.09	1.32	1.39	1.49
5		1.04	1.21	1.44
6				

Fused Bn Solution 1-Sigma from EG/KSC/SX Data

From V, To->	7	8	9	10
1				
2				
3	0.12	0.10	0.09	0.07
4	0.18	0.15	0.12	0.10
5		0.17	0.16	0.15
6				

Table 7-8. Foam impact characteristics for each data set and data start/stop number. (Courtesy Phillip Stuart JSC/EG)

and the best statistical estimate of the average ballistic number of the foam debris, which was between 1.69 and 1.04 ft/lb^2. The statistical 1-σ confidences in this process all ranged from 0.07 to 0.18 ft/lb^2.

The converged initial conditions and ballistic numbers of each data set were integrated in the Space Shuttle vicinity flow field to interpolate the characteristics of their impact on the shuttle wing. The collected results of this interpolation are found in Table7- 4. The (*x, y, z*) columns represent the impact location in ET coordinate frame in inches while the (*u, v, w*) columns represent the velocity components in the ET frame (*x, y, z*) direction in ft/sec. The *vel* column with bold characters represents the magnitude of the impact velocity in ft/sec and the *ang* column is the incidence angle of the impact in degrees where 90 degrees is normal to the surface of the impact point. The (*angxy, angxz, angyz*) columns represent the angles that a foam debris particle would impact the Shuttle wing leading edge and support alignment of a launch mechanism to simulate foam debris impact. Specifically the planes in these angles are +*xy* in the Space Shuttle up direction, +*xz* toward the starboard side, and +*yz* toward the Space Shuttle aft section. Note that data sets ES3-7 and SX3-7 did not impact the Space Shuttle. The velocity magnitudes at interpolated impact points ranged from 669 ft/sec to 853 ft/sec with incidence angles varying from 5 to 33 degrees. The impact point of each data set is represented visually in Figure 7-21.

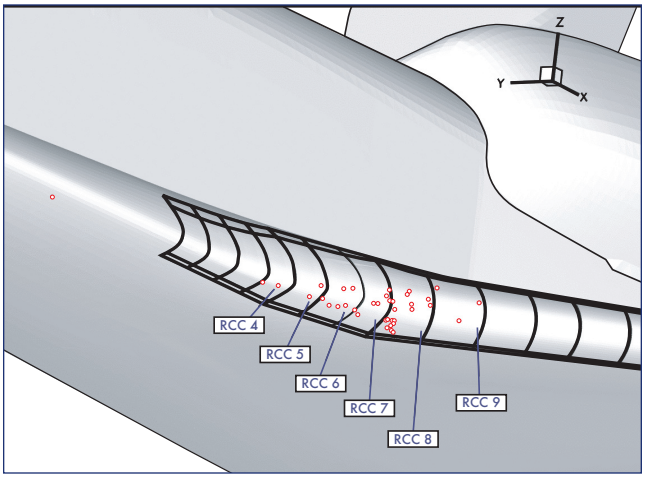

Figure 7-21. Interpolated impact points of all data sets.

7.3.1 Least Squares Analysis Conclusions

A lease squares estimation technique was used to obtain initial foam debris position and velocity and average ballistic number. An important feature of this technique is the calculation of a statistical confidence value that is generated along with the estimate which gives a probabilistic range on the estimate. With the data available, the average ballistic number of foam debris is estimated to be between 1.04 and 1.69 lb/ft^2 with a 1-σ confidence between 0.07 and 0.18 lb/ft^2 depending on the data start and stop points used in the lease squares algorithm. From Table 3, it can be seen that the average ballistic number consistently rises as the data is processed with more data end points from the latter part of the observation set. This indicates that the ballistic number of the foam debris was higher as it neared the end of its trajectory. The results from this analysis can be used to create a probabilistic description of the initial conditions and impact conditions of the foam debris trajectory. This description is based on the post-processed video foam debris impact data, the CFD flow model of the debris trajectory volume, and the inertial acceleration experienced by the Shuttle during the data record time span. Without an increase in the quantity or quality of foam debris observation data, further analysis using the least squares technique will not produce differing results of any statistical significance.

7.4 Recommendations (Condon, Lee, and Crain)

The composite list of recommendations from the analyses of Condon, Lee, and Crain, are as follows:

1. STS ascent tracking system should employ cameras with improved frame rates & reliability for improved debris tracking. Sparse data density and quality were a significant limitation in trajectory estimation.
2. There should be an accurate and consistent time stamp for the ascent video cameras.
3. More digits in the seconds readout of all camera time stamps would be useful for modeling of debris trajectories. The transit time for the STS-107 debris object was very short – less than 0.17 seconds. More precision in the readout would reduce truncation errors, which can currently be significant when modeling motion over so short a time span. At least three more digits in the readout would be useful, i.e. six digits after the decimal for the seconds readout.
4. NASA should have in place a turn-key process to analyze ascent debris events. This process should include image analysts to develop observational data, aerodynamicists to develop realistic flow conditions, and flight dynamics experts to estimate the object path,

velocities, and aerodynamic parameters. The process should include multiple disciplines and organizations.
5. The process for analysis of ascent debris trajectories analysis should include:
   a. Modeling of debris motion based on dynamics equations and CFD based flow fields.
   b. Solution of initial conditions and aerodynamic parameters to fit the debris trajectory to image analysis observations in the form of view vectors/lines.
   c. A more rigorous statistical navigation type methodology should be explored, in parallel with the current brute force approach.
6. There should be a standardized format and process for reporting image analysis debris observations for dynamics analysis:
   a. Debris observations should be reported as view lines in standard anchor point plus vector direction format, expressed in STS External Tank coordinates.
7. Analysis of debris observation view lines should consider frame-to-frame changes in STS position and orientation, i.e. view vector direction.

8.0 6-DOF Unsteady CFD Analysis

8.1 Approach

Viscous and inviscid Computational Fluid Dynamics (CFD) codes were used to carry out unsteady simulations of the coupled aerodynamic and debris motion for Columbia ascent conditions. The debris motion was allowed to translate and rotate in each coordinate direction based on the aerodynamic forces, giving it six degrees of freedom. In all, more than 40 viscous and 200 inviscid solutions were generated. The simulations examined six possible pieces of the debris (ranging in size from 166 cubic inches to 1450 cubic inches), and a range of foam mass densities (from 2.1 to 5.0 lb per cubic foot). In the simulations for both codes the initial velocity and rotation rates were varied, until an initial condition that resulted in an impact of the Orbiter wing was found. The viscous results are products of the OVERFLOW-D code, while the inviscid results are products of the CART3D code. The details of each computational approach are briefly summarized in the following sub sections.

8.2 Tool Background

OVERFLOW-D is based on version 1.6au of the NASA OVERFLOW code, but has been significantly enhanced to accommodate problems that involve bodies in relative motion. The enhancements represent in-core subroutine actuated operations, including a general 6-degrees-of-freedom (6-DOF) model, contact detection algorithms, impact reaction routines, and solution adaptation capability. A near-body/off-body domain partitioning method is used in OVERFLOW-D as the basis of problem discretization. The near-body portion of the domain is defined to include the vehicle surface geometry and the volume of space extending out a short distance. This portion of the domain is discretized with body-fitted viscous grid components. The off-body portion of the domain is defined to encompass the near-body domain and extend out to the far-field boundaries of the problem. The off-body domain is filled with a system of uniform Cartesian grids of variable levels of refinement. The off-body grids are automatically generated by OVERFLOW-D such that all near-body grids are always surrounded by off-body grid components of comparable resolution capacity. These spacing constraints are enforced at each time step for moving body applications. The SSLV near-body and off-body grid systems used for the present Columbia debris breakaway simulations consist of more than 20 million points. Each trajectory has been resolved temporally with more than 10,000 time-steps.

The Cart3D code solves the Euler equations using unstructured Cartesian meshes. Cart3D takes as input the triangulated surface geometry and generates an unstructured Cartesian volume mesh by subdividing the computational domain based upon the geometry, and any pre-specified regions of mesh refinement. In this manner, the space near regions of high surface curvature contains highly refined cells, while areas away from the geometry contain coarser cells. For moving-body problems, Cart3D's solver is based on a dual-time, implicit scheme with multigrid as a smoother on the inner iterations permitting large time steps. The package is tightly coupled with a 6-Degree-Of-Freedom (6-DOF) module so that mesh automatically adjusts as pieces of geometry move under aerodynamic loads. The efficiency of the code with coupled 6-DOF is comparable to the best codes in the literature. Cart3D has been parallelized to efficiently run on shared-memory computers on over 1000 processors. Due to the high degree of automation in the package, simulations of new vehicles can be setup in a matter of hours. Trajectory simulations for the Columbia debris cases typically ran in less than one day on 64 SGI Origin CPUs.

8.3 Observations

With this database of several hundred simulations, several general observations can be made with confidence.

1. The cross flow (Y-Z) position and cross flow velocity are relatively sensitive to release conditions. With the right initial conditions, the debris can be made to fly well above or below the Orbiter wing. Y-Z position, however, is less critical, since we know from the photographic and forensic evidence the approximate Y-Z position of the debris impact. Therefore initial conditions were chosen to give this result (wing impact near RCC panels 6-8).
2. Streamwise (X) position and velocity generally quite insensitive to release conditions (±~ 50 ft/ sec @ impact location), and are primarily dependent upon the density and size of the debris used in the simulations.
3. Of these, the final relative impact velocity shows strong dependence upon the foam density, and is less sensitive to the size and geometry of the foam piece.

8.4 Results

A trajectory that begins with a rotating forward flip (nose-down) is more likely than a backward flip (nose-up) to impact the Shuttle's lower wing leading-edge surface. A backward flip would generate significantly more lift before the

piece starts to tumble, carrying it too far outboard or over the top of the wing. In a forward-flip release, the debris leading edge is pushed down under aerodynamic loads, and begins tumbling almost immediately – experiencing little aerodynamic lift in the process. As a result the forward-flip trajectories follow the Orbiter's surface more closely, and more consistently impact the wing leading edge. Also, trajectories produced by forward-flip releases are closer to the initial positions reported by the Image Analysis Team teams.

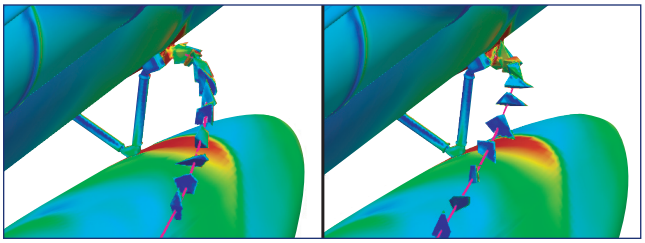

Figure 8-1. Backward vs. forward flip trajectories.

These images also illustrate the tumbling behavior of the debris after it separated from the launch vehicle. The homogeneous wedge shaped foam debris analyzed in these simulations is unstable and will tend to rotate rather than trim out in a stable attitude. To assume a stable attitude, with a correspondingly lower drag coefficient, would require a significantly different debris shape than the shape observed on the launch films or would require some additional mass embedded in the foam debris. No conclusive evidence supports this scenario.

The effect of density variation was investigated for debris pieces ranging in size from 705-1450 cubic inches. The figure below shows streamwise relative velocity of a 705 cubic inch piece as it travels downstream. This chart shows predicted impact speeds of between 1000-750 ft/sec as the foam density is varied from 2.1-5.0 lb/ft^3. While debris with different sizes and shapes had different actual impact speeds, these results are typical. For example, increasing the debris size to 1450 cubic inches only resulted in a decrease of about 100 ft/sec from the results shown in this figure. The prediction of impact velocity between the two simulation codes (Cart3D and OVERFLOW) was very consistent, with results varying by only ±50 ft/sec overall, and results for cases with similar trajectories (and impact points) varying by only 10-20 ft/sec.

Ballistic numbers were computed for the debris pieces of 705, 855, and 1450 cubic inches. The average ballistic number for a given trajectory was found to be primarily a function of the foam density. An increase in foam density results in increased ballistic number. Two figures showing the ballistic number variation as the debris tumbles downstream are included. The first of these figures show the trajectories for foam density variations on a 704 cubic inch wedge shaped debris piece. The second figure shows trajectories for a similar piece of 855 cubic inch and 2.4 lb per cubic foot foam density. These ballistic numbers were used in the correlation with the Image Analysis Team results, as described above.

The rotation rates for these trajectories were collected and are shown in the following figures.

These results are consistent with the Image Analysis assessment indicating a rotation rate of at least 18 revolutions/second and show that the rotation rate could be even higher for this smaller volume of foam.

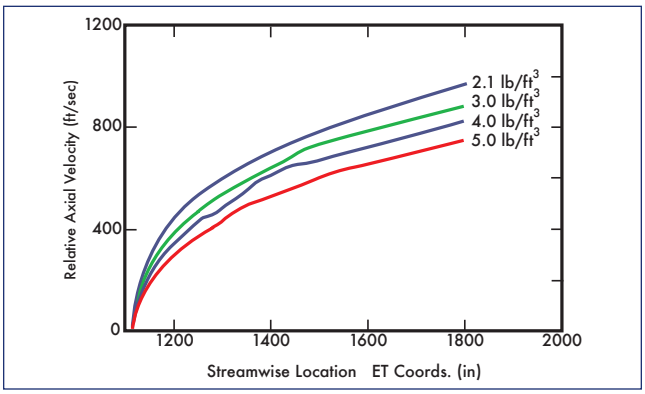

Figure 8-2. Impact velocity for various effective densities.

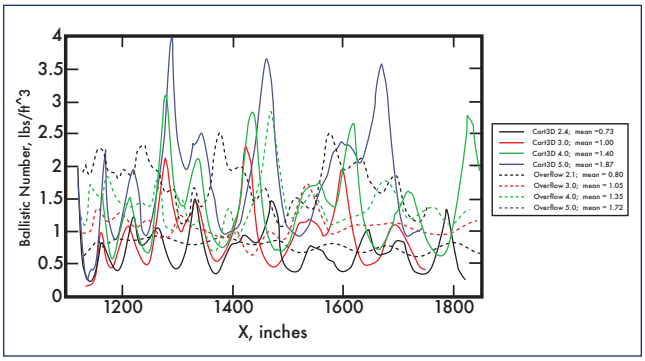

Figure 8-3. Ballistic number variation along trajectory (704 in^3 foam volume).

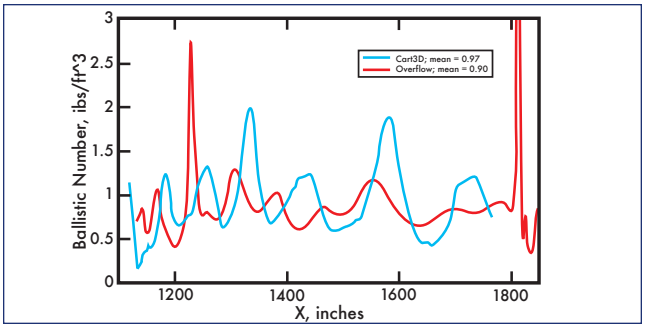

Figure 8-4. Ballistic number variation along trajectory (855 in^3 foam volume).

Axis	Rotation rate (Hz)
W1	38 ± 12
W2	[1] 1 ± 10
W3	12 ± 12

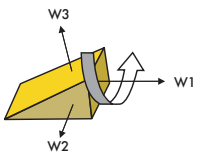

Figure 8-5. Rotation rates from unsteady CFD.

The effects of the debris on the surface pressures of the Shuttle were estimated by subtracting the steady state solution surface pressures from those computed during an unsteady trajectory computation. This analysis shows that the Orbiter leading edge pressure is lowered by approximately 0.4 psi just before the debris impact. This is shown in the following figure, which shows color contours of the difference in pressure on the surfaces.

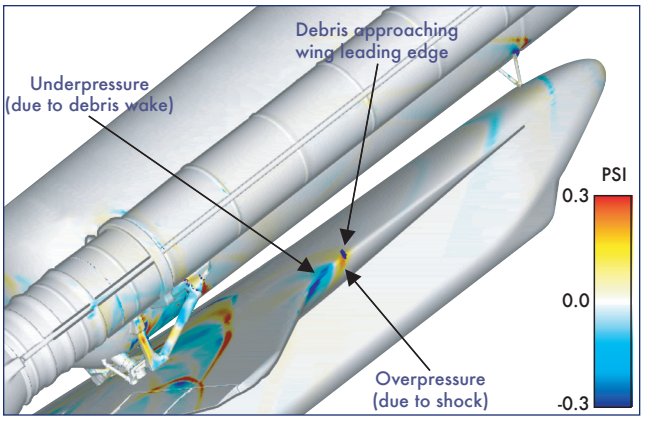

Figure 8-6. Delta pressure on vehicle surface caused by debris.

Red and yellow indicate increased pressures and cyan and blue indicate lowered local pressure. White or gray regions show small or no change in pressure. The lowered local wing surface pressure is caused by the wake of the debris piece that precedes the debris as it travels past a fixed point on the Orbiter wing. This change in local pressure may help explain the anomalous accelerations measured on the left wing outboard elevon accelerometer recorded during ascent and may explain the unusual acceleration signature seen shortly after the debris impact on the leading edge of the wing.

A similar trajectory that missed the wing leading edge and traveled near one of the two Orbiter pressure instruments that showed unusual behavior during the STS-107 launch is shown below. The debris velocity is probably somewhat higher than the debris cloud seen after the initial debris impact. The passage of the cloud of debris was too rapid for the 10 Hz pressure instrumentation to detect the effect of the debris passage but the 200 Hz accelerometer on the left wing outboard elevon could detect a pressure change of this duration. Review of the digitally enhanced launch video shows a number of large pieces of debris traveling outboard under the left wing elevon that may have caused a similar pressure change on the control surface.

The following figure shows the change in pressure near one of the anomalous taps caused by the simulated debris shape passing near the Orbiter wing without an impacting the wing leading edge. For this debris velocity the pressure oscillation occurs over approximately 0.01 seconds and realistically would not have been sensed by the 10 Hz sample rate of the pressure taps. The zero value on the x-axis is simply a reference time prior to the debris's passage near the pressure tap.

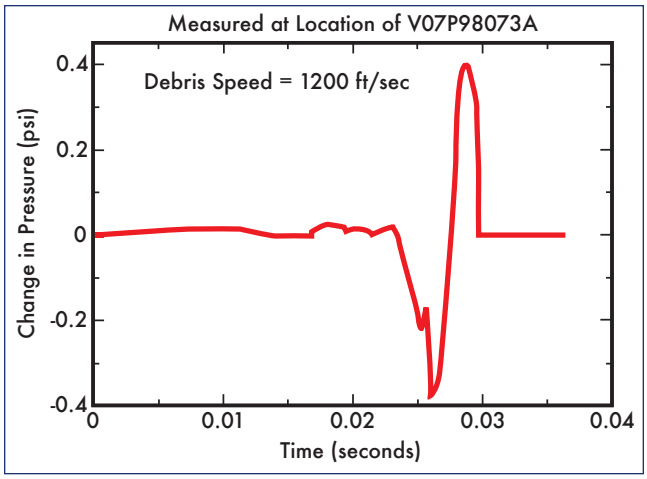

Figure 8-7. Delta pressure near orbiter lower surface pressure tap.

9.0 RCC Impact Testing Inputs

The primary goal of the impact testing on Orbiter RCC panels was to simulate, as closely as possible, the debris event on STS-107. Several aspects of this goal were difficult to achieve. Simulating the complete combined environment including external pressure loads and temperatures was not possible due to limitations in the testing setup and equipment. External pressures and temperatures from the static geometry CFD solutions were provided to the impact analysts for pre- and post test assessment purposes. Impact velocities from the trajectory analysis/ballistic number estimation were used but mass estimates and angle of incidence inputs required additional analysis.

9.1 Debris Mass Estimation

The debris mass estimates were based on the ballistic coefficient analysis results combined with the ADT program and unsteady CFD results for the 855 in^3 foam volume estimate from the External Tank Project. ADT and the unsteady CFD results predicted that the 855 in^3 foam would have a BN approximately equal to 1.0 with an impact velocity of 950 ft/sec.

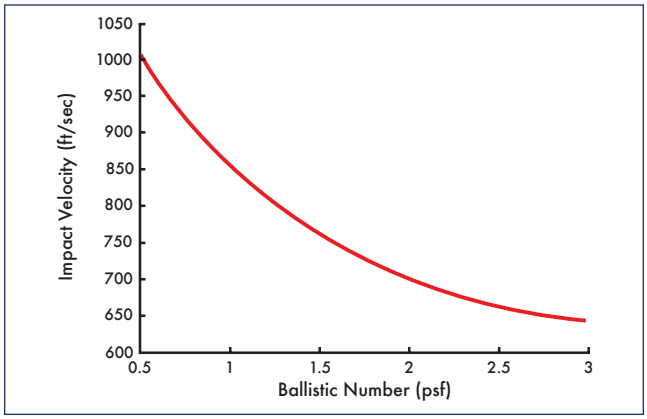

figure 9-1. impact velocity at 1,800 inches vs. ballistic number.

Ballistic number analysis of the Image Analysis trajectories estimated the most likely range of 1.2 < BN < 1.4. Due to the accelerated test schedule and lead times required to procure test article hardware a simple ratio of the predicted ballistic numbers to the baseline 855 in^3 geometry was used to predict the as tested foam weights.

Writing the ballistic number in terms of foam density results in the following equation:

$$BN = \frac{\rho_{foam}\, Volume}{C_D\, Area_{ref}}$$

Equation 9-1. Ballistic number as a function of density.

The increase in BN could have come from a number of different sources:

- Reduced drag coefficient (C_D)
- Higher effective mass
  - Due to larger volume
  - Due to embedded mass

Drag coefficient is a function of geometry and Mach number. Characterizing the drag coefficient for a tumbling object is a difficult undertaking. The best estimate of the average drag coefficient for this debris comes from the unsteady 6-DOF CFD results. These codes predicted a C_D of 1.67 for the baseline shape from the ET Project, using a reference area equal to one fifth of the foam surface area. Comparing this value to experimental data from a number of different sources, using consistent reference area definitions did not support a large reduction in this value that would account for the BN number increase.

The ET Project did not support any significant added mass scenarios involving ice or SLA embedded in the foam and the Project's largest estimated weight of the debris was 1.3 lb.

Considering these inputs, along with the larger potential volume of a smaller ramp angle discussed in Section 4, the judgment was made that a larger foam volume could have come from the bipod ramp.

9.2 Angle of Incidence Inputs

The angle of incidence inputs were provided relative to the impact test RCC test article. The data was provided in this format to simplify the aiming procedure in the test and to allow the structural analysts to choose any point on the RCC surface as their target. The curvature of the Orbiter wing leading edge and the size of the debris make specific angle of incidence estimates difficult. The following figure shows the intersection of a debris trajectory with the wing leading edge along with an estimated "footprint" due to the debris impact. This illustrates the range of impact angles that are possible for a specific impact predicted by one of the Image Analysis Team members.

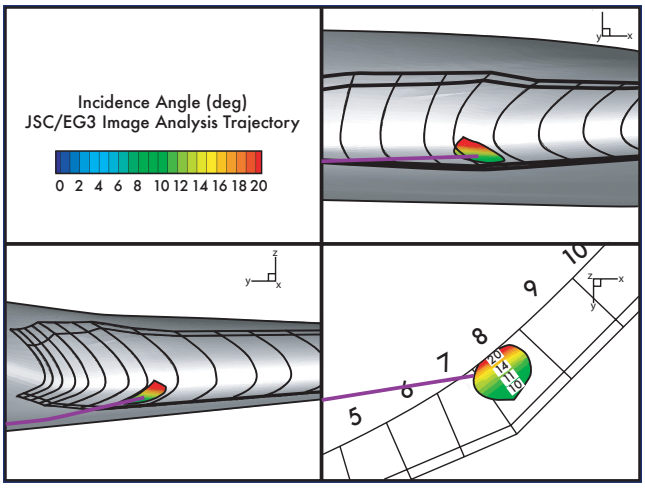

Figure 9-2. Angle of incidence on RCC panel (1 foot radius footprint).

The final incidence angle range was determined based the range predicted debris trajectory impacts on RCC Panel 8 from the trajectory analysis analysts. The terminal velocity vectors for these trajectories were extracted and the vector's angles relative to the test article coordinate system were calculated. The results are shown in the following two figures.

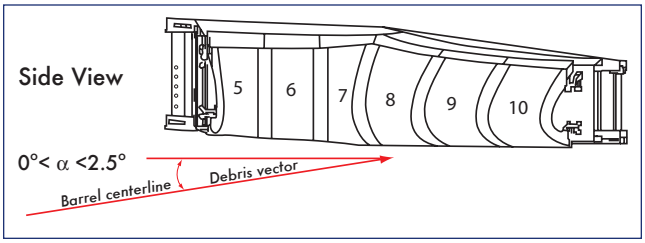

Figure 9-3. Impact test article rotation about Y-axis.

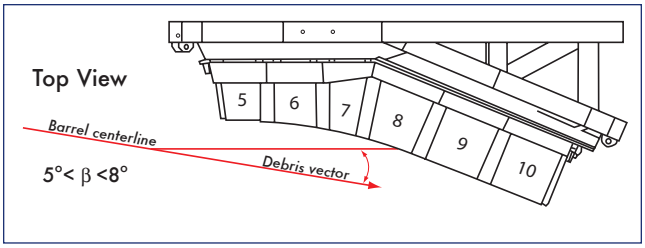

Figure 9-4. Impact test article rotation about Z-axis.

Bold values indicate more conservative angles that would result in higher energy normal to the test article.

10.0 Conclusions/Recommendations

10.1 Image Analysis

The Columbia Accident Investigation Board has made a number of recommendations in this area that are consistent with the recommendations made by the trajectory analysis/ ballistic number estimation analysts in Section 7.

The application of physics-based trajectory analysis techniques to the Image Analysis trajectories clearly showed their capability to improve the debris impact velocity estimates. Additionally these techniques can provide insight into the mass of observed debris and physics based trajectory extrapolations where multiple views are not available. A turnkey system including this capability could significantly reduce the uncertainty associated with determining ascent debris mass and trajectories.

Worst-case debris impacts occur in a flow regime that generates a number of strong shock waves. These shocks can cause optical distortions that might mislead image analysts. Portions of the STS-107 debris trajectory were probably distorted by the density gradients caused by these shock waves and resulted in higher uncertainties in these areas. Simulating these distortions using CFD tools could provide insight into the magnitude of these distortions and improve the quality of the Image Analysis products.

10.2 Debris Transport

The current Ascent Debris Trajectory Program provided estimates were very close to the final investigation recommendations for debris mass and impact velocity. However, due to inefficiencies in the code and errors in the code's implementation the Ascent Debris Transport code has been completely rewritten. The new code is currently undergoing verification and validation testing.

Unsteady 6-DOF CFD solutions provided valuable insight into aerodynamic and debris dynamics that would have been difficult or impossible to obtain by any other means. These tools are being utilized to better characterize tumbling debris aerodynamics and to assess the assumptions made in the current debris transport code. These results will be used to update the debris transport code and to improve the accuracy of its predictions.

11.0 Acknowledgements

The authors would like to acknowledge the outstanding support provided by the NASA Advanced Supercomputing Division and Silicon Graphics, Inc. Without the dedicated access and support they provided throughout the investigation many of the required analyses could not have been accomplished in a timely manner.

Additionally we would like to acknowledge all of the individuals and companies that volunteered their time and resources to support this effort.

Most of the NASA Ames Research Center members of this team were coworkers of Kalpana Chawla prior to her acceptance as an astronaut candidate. She will be missed.

12.0 References

1-1 G. J. Byrne and C. A. Evans, "STS-107 Image Analysis Team Final Report," NSTS-37384, June 30, 2003.

1-2 Joint Scenarios Report, July 8, 2003.

5-1 D.C. Jespersen, T.H. Pulliam, and P.G. Buning, "Recent Enhancements to OVERFLOW," AIAA-97-0644, AIAA 35th Aerospace Sciences Meeting, Reno, NV, Jan. 1997. http://science.nas.nasa.gov/~jesperse/papers/aiaa97-0644.ps.Z

2-2 P.G. Buning, D.C. Jespersen, T.H. Pulliam, G.H. Klopfer, W.M. Chan, J.P. Slotnick, S.E. Krist, and K.J. Renze, "OVERFLOW User's Manual, Version 1.8s," NASA Langley Research Center, Nov. 2000.

2-3 D. G. Pearce, et al, "Development of a Large Scale Chimera Grid System for the Space Shuttle Launch Vehicle," AIAA-93-0533-CP, January 1993.

2-4 J. P. Slotnick, et al, "Navier-Stokes Simulation of the Space Shuttle Launch Vehicle Flight Transonic Flowfield Using a Large Scale Chimera Grid System," AIAA-94-1860, June 1994.

2-5 R. J. Gomez, E. C. Ma, "Validation of a Large Scale Chimera Grid System for the Space Shuttle Launch Vehicle," AIAA 94-1859.

6-1 J.W. McClymonds, J.J. Baumbach, R.R. Cassas, L.B. Grassi, J. M. Kelleher, "Space Shuttle Debris Data Book," SSD95D0193-Rev A, November 2000.

6-2 Dr. Ing. S.F. Hoerner, "Fluid Dynamic Drag," Hoerner Fluid Dynamics, 1964.

13.0 Appendix A

13.1 Acronyms and Abbreviations

6-DOF	6 Degrees Of Freedom (3 forces + 3 moments)
ADTP	Ascent Debris Transport Program
CFD	Computational Fluid Dynamics
ET	External Tank
KSC	Kennedy Space Center
MET	Mission Elapsed Time
MSFC	Marshall Space Flight Center
NASA	National Aeronautics and Space Administration
RCC	Reinforced Carbon Carbon
SLA	Super-Lightweight Ablator
SRB	Solid Rocket Booster
SSLV	Space Shuttle Launch Vehicle
STS	Space Transportation System

14.0 Appendix B

14.1 Bipod Ramp Airloads

A key concern of the investigation was whether external air loads caused or contributed to the failure of the foam ramp resulting in the debris release. A number of static CFD runs were performed at STS-107 ascent conditions and compared to design certification loads and air loads at STS-107 conditions predicted using the engineering techniques used to design the bipod ramps. The engineering results consistently bounded the CFD analysis indicating that the design certification loads were conservative and did not under predict the actual load environments.

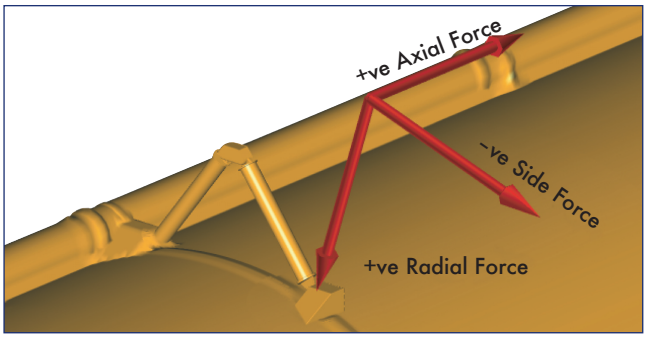

Figure 14-1. Bipod ramp force convention.

These calculations follow the engineering methodology used to predict airloads on the bipod ramps. This process integrates (pressure – freestream pressure) over the ramp surfaces to determine the aerodynamic forces acting on the ramp. The actual forces, for a perfectly bonded ramp without any venting, can be predicted by simply integrating pressures on the ramp exposed surfaces.

The following figures show the calculated loads on the –Y, or left-hand, bipod ramp. The design requirement curve is based on a high dynamic pressure trajectory designed to fly

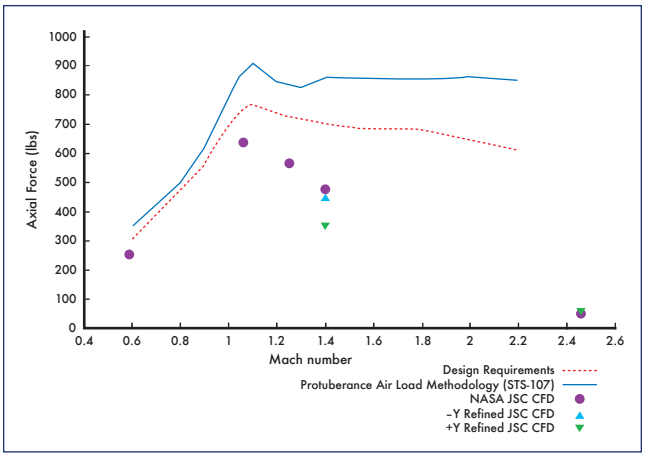

Figure 14-2. -Y Bipod ramp axial force vs. Mach number.

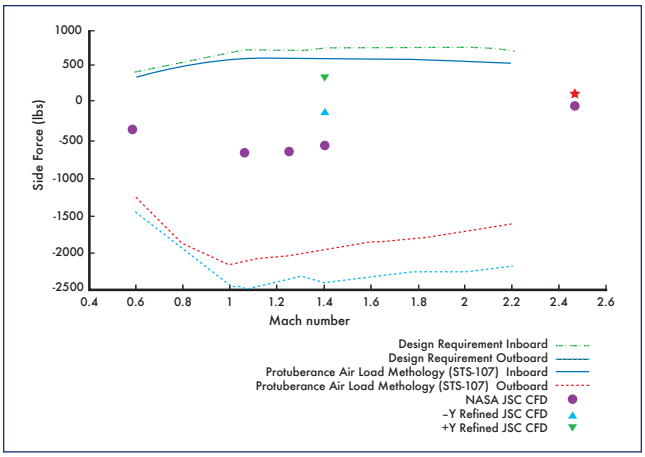

Figure 14-3. -Y bipod ramp side force vs. Mach number.

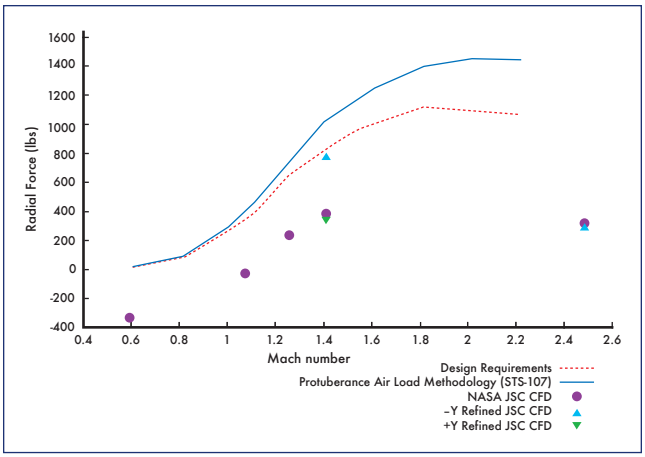

Figure 14-4. -Y Bipod ramp radial force vs. Mach number.

at the Shuttle structural design limits. The STS-107 curve uses the same analysis procedure but uses the STS-107 trajectory dynamic pressures to compute the various loads. The NASA JSC CFD symbols were computed using a simplified geometry that did not included the External Tank Intertank Stringers. The Refined JSC CFD symbols are for an updated CFD geometry that includes the stringers and refined +Y ramp geometry.

By definition positive radial force acts towards the External Tank centerline, which would tend to press the ramp down onto the External Tank surface. The bipod ramp deflects the oncoming air upward resulting in a net force that holds the ramp on to the ET.

This analysis shows that the air loads were within the design envelope and implies that a ramp with no flaws would not fail due to air loads alone. Internal voids could contain gas at atmospheric pressure that would results in local failures when the delta pressure between the gas voids and the external pressure exceeds the strength of the foam insulation. Information from the ET Project indicates that internal flaws could significantly reduce the foam strength and that cryogenic temperatures would cause a further reduction in strength.

[continued on next page]

15.0 Appendix C

15.1 Time-dependent position data sets from JSC/ES, JSC/SX, KSC and JSC/EG

JSC/ES Reference Data

Point	Elapsed Time	XET	YET	ZET	Rho	VelX	VelY	VelZ	Speed of Sound
	Sec	inches	inches	inches	slug/ft3	ft/sec	ft/sec	ft/sec	ft/sec
1	0	1115	-65	581	2.32387E-04	1375.187	-410.57	-137.074	1256.976
2	0.017	1125	-89	581	2.07126E-04	1737.851	-53.0254	-216.018	1169.928
3	0.033	1136	-117	581	2.68687E-04	1967.677	-160.848	16.28692	1088.297
4	0.05	1141	-139	585	2.73989E-04	1941.608	-245.992	40.81452	1094.212
5	0.066	1204	-170	597	2.39994E-04	2060.441	-294.194	-23.2117	1047.247
6	0.083	1259	-174	604	2.03557E-04	2138.5	-263.008	-26.0106	1017.069
7	0.1	1314	-175	611	1.91290E-04	2165.326	-277.616	-79.9681	1004.108
8	0.117	1439	-182	623	1.43675E-04	2288.054	-167.191	-91.8438	952.4276
9	0.133	1556	-190	625	1.42941E-04	2282.208	-195.35	-70.863	954.579
10	0.15	1668	-190	625	1.70959E-04	2202.615	-132.83	91.80206	993.5049
11	0.167	1787	-193	625	1.83534E-04	2148.811	-122.726	-0.39817	1021.162

JSC/SX Reference Data

Point	Elapsed Time	XET	YET	ZET	Rho	VelX	VelY	VelZ	Speed of Sound
	Sec	inches	inches	inches	slug/ft3	ft/sec	ft/sec	ft/sec	ft/sec
1	0	1112.5	-43.895	573.58	2.16640E-04	49.46285	-177.988	334.6481	1395.33
2	0.017	1127.2	-80.441	575.46	1.97820E-04	1334.217	-453.177	-444.755	1242.135
3	0.033	1125.3	-96.702	581.41	2.14074E-04	1887.878	94.9397	-74.6841	1120.574
4	0.05	1160.9	-138.38	581.03	2.54430E-04	1999.954	-216.817	-2.25609	1074.105
5	0.066	1187.7	-140.11	586.3	2.33491E-04	2050.208	-190.261	-26.3199	1056.017
6	0.083	1244.5	-133.37	597.91	2.17631E-04	2079.32	-243.409	-84.3914	1042.191
7	0.1	1308.1	-138.1	610.19	1.71978E-04	2197.666	-190.632	-82.8541	994.2547
8	0.117	1440.2	-165.52	614.38	1.41428E-04	2284.71	-183.007	-105.64	953.4332
9	0.133	1553.2	-181.13	617.4	1.40716E-04	2285.151	-202.576	-83.9461	952.8312
10	0.15	1684.1	-192.93	618.05	1.74800E-04	2202.278	-116.505	91.05107	994.2049
11	0.167	1814.2	-210.69	618.63	1.73565E-04	1882.989	-25.157	-278.549	1113.49

KSC Reference Data

Point	Elapsed Time	XET	YET	ZET	Rho	VelX	VelY	VelZ	Speed of Sound
	Sec	inches	inches	inches	slug/ft3	ft/sec	ft/sec	ft/sec	ft/sec
1	0	1133	-58	575.5	1.69402E-04	878.0123	-495.741	166.5922	1325.663
2	0.015	1139	-79	580.5	2.46196E-04	1802.137	-317.569	-321.847	1130.33
3	0.031	1149	-104	583.5	2.35645E-04	2037.209	24.80037	-91.2693	1066.995
4	0.047	1168	-126	585.5	2.37981E-04	2037.508	-131.667	-4.29115	1062.876
5	0.062	1198	-135	592.5	2.29344E-04	2053.935	-169.072	-25.681	1055.481
6	0.078	1244	-144	601.5	2.16592E-04	2083.916	-271.009	-48.178	1039.217
7	0.093	1323	-162	611.5	1.78214E-04	2192.271	-234.635	-84.5304	994.4348
8	0.109	1416	-173	620.5	1.47391E-04	2272.257	-178.868	-91.3495	959.7419
9	0.125	1524	-186	617.5	1.43629E-04	2281.069	-206.015	-86.8857	954.4202
10	0.14	1634	-194	620.5	1.63414E-04	2231.948	-127.52	45.20563	981.0337
11	0.166	1787	-207	620.5	2.37158E-04	2002.997	-301.408	-339.699	1058.553

JSC/EG Reference Data Set

Point	Elapsed Time	XET	YET	ZET	Rho	VelX	VelY	VelZ	Speed of Sound
	Sec	inches	inches	inches	slug/ft3	ft/sec	ft/sec	ft/sec	ft/sec
1	0.000	1130.7	-61.0	571.0	1.68679E-04	961.8044	-395.291	124.0708	1320.115
2	0.017	1123.9	-75.3	576.6	2.03591E-04	1220.147	-555.456	-366.008	1263.976
3	0.033	1145.7	-108.7	579.3	2.26083E-04	2023.392	29.45869	-17.7892	1072.062
4	0.050	1137.2	-116.3	586.6	2.61401E-04	1993.299	-127.235	16.73082	1079.331
5	0.066	1186.2	-128.4	593.1	2.33698E-04	2043.497	-144.773	-17.5247	1060.271
6	0.066	1186.2	-128.4	593.1	2.33698E-04	2043.497	-144.773	-17.5247	1060.271
7	0.100	1323.7	-144.2	608.9	1.67756E-04	2211.619	-187.739	-91.1938	987.9354
8	0.117	1481.6	-172.4	611.7	1.43627E-04	2275.56	-219.244	-100.71	956.3618
9	0.133	1570.6	-186.1	614.9	1.43774E-04	2282.363	-180.533	-72.9557	955.274
10	0.150	1674.5	-201.4	618.3	1.74779E-04	2210.775	-103.87	103.0063	990.4358
11	0.166	1806.8	-220.9	622.6	2.47921E-04	1936.095	-299.572	-425.604	1079.068

15.2 Time-dependent ground camera view vector data sets

Appendix E.2.a Composite data – Interleaved data for Camera 208 and 212 based on original view vector data obtained from MSFC. Included are anchor locations (x0, y0, z0, x1, y1, z1) for time dependent view vectors for cameras 208 and 212. Also included is the estimated error (in inches) associated with each view vector.

Index	Time (sec)	x0 (inches)	y0 (inches)	z0 (inches)	x1 (inches)	y1 (inches)	z1 (inches)	Camera	Error
1	0.000	2102.9500	-500.0130	671.9760	1125.8000	-61.2923	576.4040	212	8.2000
2	0.004	1774.2600	-499.9580	438.0427	1169.6900	-86.6527	552.9080	208	18.5962
3	0.016	2063.2600	-500.0000	668.3100	1128.8700	-80.6685	576.6020	212	8.2000
4	0.021	1733.1600	-499.9600	454.6232	1157.7400	-106.7230	563.7380	208	23.5915
5	0.032	2019.4000	-499.9870	669.1120	1140.0200	-105.4980	582.6850	212	8.2000
6	0.038	1703.1000	-499.9610	474.8298	1149.8500	-122.0140	579.5370	208	20.3733
7	0.047	1991.2600	-499.9910	664.9740	1148.8200	-122.2180	581.9860	212	8.2000
8	0.054	1691.7400	-499.9620	473.6517	1193.8200	-159.9260	567.7090	208	16.3291
9	0.063	1996.1300	-500.0000	667.8960	1177.6700	-133.1250	587.0760	212	8.2000
10	0.071	1721.4100	-499.9610	485.8514	1217.4800	-155.8150	581.0500	208	20.4872
11	0.078	2022.3800	-500.0000	676.9680	1194.0700	-128.7940	594.9300	212	8.2000
12	0.094	2062.1900	-499.9890	683.0460	1287.5000	-152.9570	606.1940	212	8.2000
13	0.110	2133.6600	-499.9950	686.6290	1355.0700	-151.3240	609.2000	212	8.2000
14	0.121	1881.0300	-499.9590	528.1820	1381.1200	-158.9790	621.9050	208	18.3798
15	0.125	2210.3600	-499.9910	685.3920	1483.8500	-174.7320	612.9710	212	8.2000
16	0.138	2000.6600	-499.9570	531.9460	1524.4400	-175.2120	621.0590	208	20.3733
17	0.141	2282.3900	-500.0110	690.6460	1576.7600	-184.1750	620.0830	212	8.2000
18	0.154	2128.0600	-499.9530	537.7890	1638.4800	-166.1720	629.2390	208	19.9629
19	0.171	2202.7100	-499.9520	553.5490	1817.9400	-237.7020	625.1690	208	19.6575

Appendix E.2.b Composite data – Interleaved data for camera 208 and 212 with camera 208 time data shifted up (earlier) by 6.75 millisecond. This data set is consistent with the time shift that MSFC claimed provided the best "triangulation" of the image data. Included are anchor locations (x0, y0, z0, x1, y1, z1) for time dependent view vectors for cameras 208 and 212. Also included is the estimated error (in inches) associated with each view vector.

Index	Time (sec)	x0 (inches)	y0 (inches)	z0 (inches)	x1 (inches)	y1 (inches)	z1 (inches)	Camera	Error
1	0.00000	1774.2600	-499.9580	438.0427	1169.6900	-86.6527	552.9080	208	18.5962
2	0.00275	2102.9500	-500.0130	671.9760	1125.8000	-61.2923	576.4040	212	8.2000
3	0.01700	1733.1600	-499.9600	454.6232	1157.7400	-106.7230	563.7380	208	23.5915
4	0.01875	2063.2600	-500.0000	668.3100	1128.8700	-80.6685	576.6020	212	8.2000
5	0.03400	1703.1000	-499.9610	474.8298	1149.8500	-122.0140	579.5370	208	20.3733
6	0.03475	2019.4000	-499.9870	669.1120	1140.0200	-105.4980	582.6850	212	8.2000
7	0.04975	1991.2600	-499.9910	664.9740	1148.8200	-122.2180	581.9860	212	8.2000
8	0.05000	1691.7400	-499.9620	473.6517	1193.8200	-159.9260	567.7090	208	16.3291
9	0.06575	1996.1300	-500.0000	667.8960	1177.6700	-133.1250	587.0760	212	8.2000
10	0.06700	1721.4100	-499.9610	485.8514	1217.4800	-155.8150	581.0500	208	20.4872
11	0.08075	2022.3800	-500.0000	676.9680	1194.0700	-128.7940	594.9300	212	8.2000
12	0.09675	2062.1900	-499.9890	683.0460	1287.5000	-152.9570	606.1940	212	8.2000
13	0.11275	2133.6600	-499.9950	686.6290	1355.0700	-151.3240	609.2000	212	8.2000
14	0.11700	1881.0300	-499.9590	528.1820	1381.1200	-158.9790	621.9050	208	18.3798
15	0.12775	2210.3600	-499.9910	685.3920	1483.8500	-174.7320	612.9710	212	8.2000
16	0.13400	2000.6600	-499.9570	531.9460	1524.4400	-175.2120	621.0590	208	20.3733
17	0.14375	2282.3900	-500.0110	690.6460	1576.7600	-184.1750	620.0830	212	8.2000
18	0.15000	2128.0600	-499.9530	537.7890	1638.4800	-166.1720	629.2390	208	19.9629
19	0.16700	2202.7100	-499.9520	553.5490	1817.9400	-237.7020	625.1690	208	19.6575

15.3 Time-dependent ground camera view vector data sets

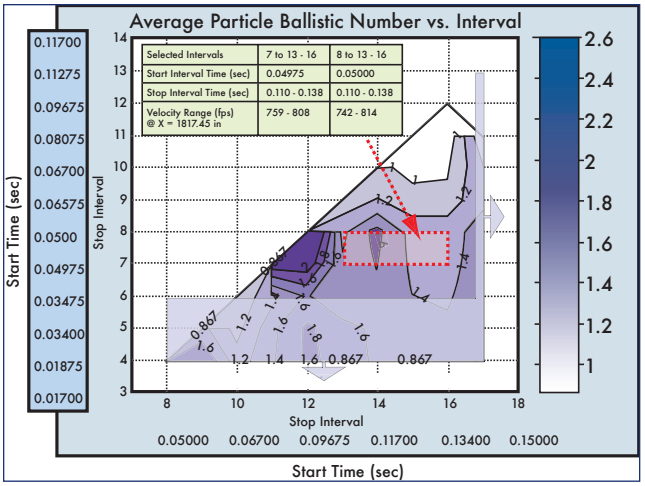

Figure 15-1. Contour plot of foam debris ballistic number vs. start and stop intervals, based on view vector data compare.

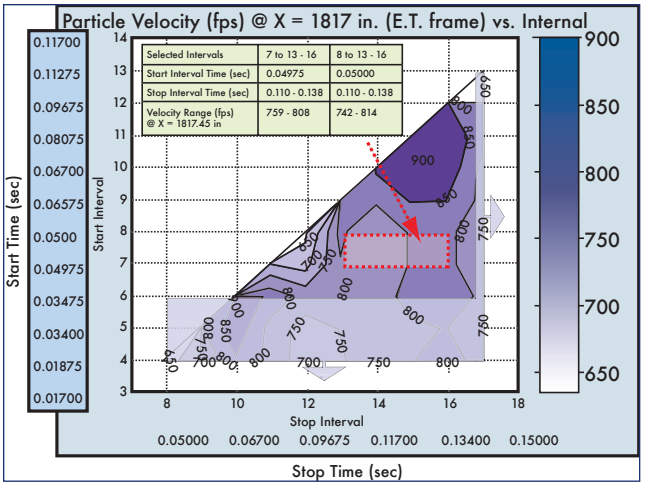

Figure 15-2. Contour plot of foam debris projected impact velocity at X = 1817.45 inches vs. start and stop intervals, based on view vector data compare.

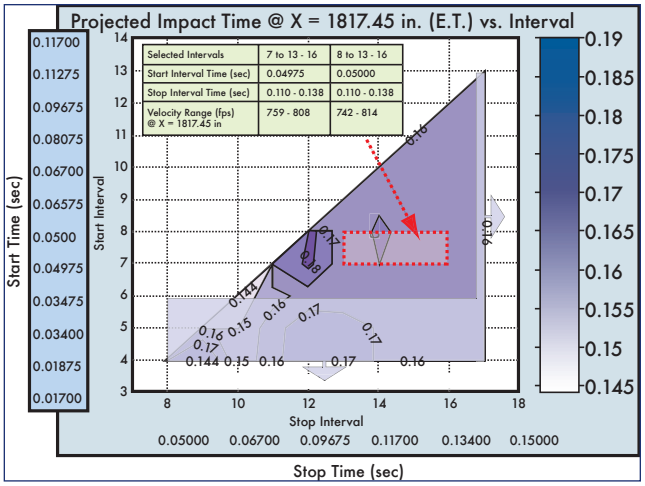

Figure 15-3. Contour plot of foam debris projected impact time at X = 1817.45 inches vs. start and stop intervals, based on view vector data compare.

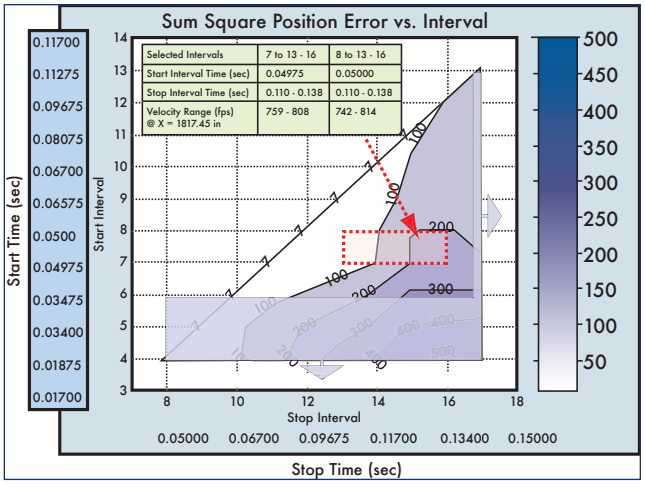

Figure 15-4. Contour plot of sum square position error between integrated trajectory and view vectors vs. start and stop intervals, based on view vector data compare.

ENDNOTES FOR APPENDIX D.8

1 Lee later performed trajectory analysis including the lift vector.

2 The trajectory is propagated beyond the optimized index interval to the Shuttle impact point using the local velocity flow grid provided by JSC/EG3. In one case (index range 8-13), the trajectory data was extrapolated about 10 inches beyond the 1817.45 X-position propagation target.